

# 1 The rich meteorology of Jezero crater over the first 250 sols of 2 Perseverance on Mars

3  
4 Rodriguez-Manfredi, J.A.<sup>1\*</sup>, de la Torre Juarez, M.<sup>2\*</sup>, Sanchez-Lavega, A.<sup>3\*</sup>, Hueso, R.<sup>3</sup>,  
5 Martinez, G.<sup>4</sup>, Lemmon, M.T.<sup>5</sup>, Newman, C.E.<sup>6</sup>, Munguira, A.<sup>3</sup>, Hieta, M.<sup>7</sup>, Tamppari, L.K.<sup>2</sup>,  
6 Polkko, J.<sup>7</sup>, Toledo, D.<sup>8</sup>, Sebastian, E.<sup>1</sup>, Smith, M.D.<sup>9</sup>, Jaakonaho, I.<sup>7</sup>, Genzer, M.<sup>7</sup>, De  
7 Vicente-Retortillo, A.<sup>1</sup>, Viudez-Moreiras, D.<sup>1</sup>, Ramos, M.<sup>10</sup>, Saiz-Lopez, A.<sup>11</sup>, Lepinette,  
8 A.<sup>1</sup>, Wolff, M.<sup>5</sup>, Sullivan, R.J.<sup>12</sup>, Gomez-Elvira, J.<sup>1</sup>, Apestigue, V.<sup>8</sup>, Conrad, P.G.<sup>13</sup>, Del Rio-  
9 Gaztelurrutia, T.<sup>3</sup>, Murdoch, N.<sup>14</sup>, Arruego, I.<sup>8</sup>, Banfield, D.<sup>15</sup>, Boland, J.<sup>2</sup>, Brown, A.J.<sup>16</sup>,  
10 Ceballos, J.<sup>17</sup>, Dominguez-Pumar, M.<sup>18</sup>, Espejo, S.<sup>17</sup>, Fairen, A.<sup>1</sup>, Ferrandiz, R.<sup>1</sup>, Fischer,  
11 E.<sup>19</sup>, Garcia-Villadangos, M.<sup>1</sup>, Gimenez, S.<sup>1</sup>, Gomez-Gomez, F.<sup>1</sup>, Guzewich, S.D.<sup>9</sup>, Harri,  
12 A.<sup>7</sup>, Jimenez, J.J.<sup>8</sup>, Jimenez, V.<sup>18</sup>, Makinen, T.<sup>7</sup>, Marin, M.<sup>1</sup>, Martin, C.<sup>1</sup>, Martin-Soler, J.<sup>1</sup>,  
13 Molina, A.<sup>1</sup>, Mora-Sotomayor, L.<sup>1</sup>, Navarro, S.<sup>1</sup>, Peinado, V.<sup>1</sup>, Perez-Grande, I.<sup>20</sup>, Pla-  
14 Garcia, J.<sup>1</sup>, Postigo, M.<sup>1</sup>, Prieto-Ballesteros, O.<sup>1</sup>, Rafkin, S.C.R.<sup>21</sup>, Richardson, M.I.<sup>6</sup>,  
15 Romeral, J.<sup>1</sup>, Romero, C.<sup>1</sup>, Runyon, K.<sup>22</sup>, Savijarvi, H.<sup>7</sup>, Schofield, J.T.<sup>2</sup>, Torres, J.<sup>1</sup>, Urqui,  
16 R.<sup>1</sup>, Zurita, S.<sup>1</sup> and the MEDA team.

17  
18 \*Corresponding authors

19  
20 <sup>1</sup>Centro de Astrobiología (INTA-CSIC), Madrid, Spain

21 <sup>2</sup>Jet Propulsion Laboratory, California Institute of Technology, Pasadena, CA, USA

22 <sup>3</sup>Universidad del País Vasco (UPV/EHU), Bilbao, Spain

23 <sup>4</sup>Lunar and Planetary Institute, Houston, TX, USA

24 <sup>5</sup>Space Science Institute, Boulder, CO, USA

25 <sup>6</sup>Aeolis Corporation, Sierra Madre, CA, USA

26 <sup>7</sup>Finnish Meteorological Institute, Helsinki, Finland

27 <sup>8</sup>Instituto Nacional de Técnica Aeroespacial (INTA), Madrid, Spain

28 <sup>9</sup>NASA Goddard Space Flight Center, Greenbelt, MD, USA

29 <sup>10</sup>Universidad de Alcalá, Alcalá de Henares, Spain

30 <sup>11</sup>Institute of Physical Chemistry Rocasolano, CSIC, Madrid, Spain

31 <sup>12</sup>Cornell University, Ithaca, NY, USA

32 <sup>13</sup>Carnegie Institution, Washington, DC, USA

33 <sup>14</sup>SAE-SUPAERO, Université de Toulouse, France

34 <sup>15</sup>NASA Ames Research Center, Mountain View, CA, USA

35 <sup>16</sup>Plancius Research, MD, USA

36 <sup>17</sup>Instituto de Microelectrónica de Sevilla (US-CSIC), Seville, Spain

37 <sup>18</sup>Universidad Politécnica de Cataluña, Barcelona, Spain

38 <sup>19</sup>University of Michigan, Ann Arbor, MI, USA

39 <sup>20</sup>Universidad Politécnica de Madrid, Madrid, Spain

40 <sup>21</sup>Southwest Research Institute Boulder, CO, USA

41 <sup>22</sup>John Hopkins APL, Laurel, MD, USA

## 42 43 **Abstract**

44  
45 Perseverance's *Mars Environmental Dynamics Analyzer* (MEDA) is collecting data at  
46 Jezero Crater, characterizing the physical processes in the lowest layer of the  
47 atmosphere as no previous instrument did before. Here we show that temperature

48 measurements at four heights capture the response of the atmospheric surface layer to  
49 multiple phenomena. We observe the transition from a stable nighttime thermal  
50 inversion to a diurnal, highly turbulent convective regime, with large vertical thermal  
51 gradients, and where local surface properties (such as Thermal Inertia) play an essential  
52 role. Recording multiple daily optical depths yielded higher aerosol concentrations in  
53 the morning than in the afternoon. Measured wind patterns are mainly driven by local  
54 topography, with a small contribution from regional winds. Daily and seasonal variability  
55 of relative humidity shows a complex hydrologic cycle. These observations raise new  
56 puzzles in which changes in surface albedo and thermal inertia may play an influential  
57 role. On a larger scale, surface pressure shows typical signatures of gravity waves and  
58 baroclinic eddies in a part of the seasonal cycle characterized before as low wave  
59 activity. These observations, combined and simultaneous, show the rich Jezero's  
60 meteorology, and unveil the diversity of processes driving change on today's Martian  
61 surface.

62

## 63 **MAIN TEXT**

64

### 65 **Introduction**

66

67 The Perseverance rover landed on 18 February, 2021, at 18.44°N 77.45°E, near the  
68 northwest rim of Jezero crater, on the inner northwest slopes of Isidis Planitia [1].  
69 Onboard the rover is the most complete environmental station sent to date to another  
70 planet: the MEDA instrument [2]. It includes new capabilities, compared to previous  
71 missions [3-8], that enable better characterization of the diversity of physical processes  
72 driving near-surface environmental changes on Jezero. MEDA acquires data  
73 autonomously, on a regular and configurable basis, in sessions that typically cover more  
74 than 50% of a sol. Sampling sessions, typically 1-hour long, alternate every sol between  
75 even and odd hours, allowing for a complete characterization of daily and seasonal  
76 cycles every other sol (Extended Data Fig. 1 shows the temporal coverage of the  
77 measurements made). MEDA also provides context for the investigations that other  
78 rover instruments and systems are conducting, and supports the planning of Ingenuity  
79 flights, as well as landing of a possible future mission to return samples collected by  
80 Perseverance.

81

82 Here we present results for the first 250 sols of the mission (solar longitudes  $L_s=6^\circ$ -121°),  
83 i.e. Northern Hemisphere Spring to early Summer.

84

### 85 **The active Atmospheric Surface Layer**

86

87 The Atmospheric Surface Layer (ASL) is the lower part of the atmosphere in direct  
88 interaction with the surface, having a depth that varies on Mars from a few meters  
89 during daytime to tens of meters at night. In the ASL, energy and mass exchanges  
90 between surface and atmosphere occur and, additionally, its hydrological cycle provides  
91 constraints on the photochemistry of surface and near-surface air. Most of the  
92 atmospheric dynamics in this layer is driven by radiative processes [9]. Albedo, net  
93 radiative flux, and Thermal Inertia (TI) are key elements of that forcing, and result in the  
94 radiative Surface Energy Budget (SEB). MEDA's Thermal Infrared Sensor (TIRS) and

95 Radiation and Dust Sensor (RDS) enable for the first time to quantify all SEB terms on  
 96 the surface of Mars (Fig. 1a), an important step in improving the predictive capabilities  
 97 of numerical models.

98

99 When Perseverance is parked every sol, TI is obtained by minimizing the difference  
 100 between measured and numerically-simulated values of the diurnal amplitude of  
 101 ground temperature (Fig. 1b). The MEDA-derived TI values range from 200 to 600  $\text{J}\cdot\text{m}^{-2}\cdot\text{K}^{-1}\cdot\text{s}^{-1/2}$ ,  
 102 as in Gale [10]. The surface albedo (Fig. 1d) is inferred for the first time so close  
 103 to the surface from the downwelling (0.2–1.2  $\mu\text{m}$ ) and reflected (0.3–3  $\mu\text{m}$ ) solar flux,  
 104 observed with TIRS (Fig. 1c,e,f). A radiative transfer model, COMIMART [11], is used to  
 105 convert both fluxes to 0.2–5  $\mu\text{m}$ . The SEB is then measured and used as an upper  
 106 boundary condition to solve the heat conduction equation for homogeneous terrains in  
 107 models [12–13]. Fig. 1a,b shows a diurnal cycle of retrieved fluxes, surface forcing and  
 108 surface temperature.

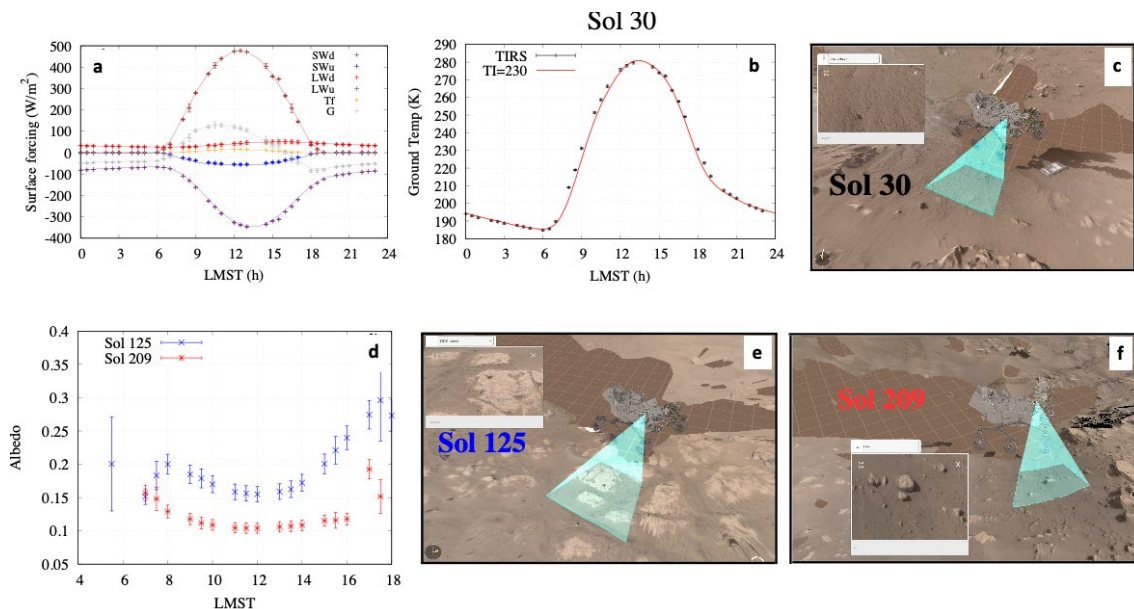
109

110 Fig. 1d shows the diurnal evolution of measured albedo on sols 125 and 209, where the  
 111 minimum value is reached near noon, and increases as solar zenith angle (SZA)  
 112 approaches  $90^\circ$ . The relative maximum at  $\sim 08:00$  and  $\sim 17:00$  occurs when  $\text{SZA} \sim 55^\circ$  and  
 113 the specular reflection is within TIRS field-of-view (FoV). This behavior points to non-  
 114 Lambertian albedo at the surface, not observable from surface satellites in nadir  
 115 pointing.

116

117 Importantly, modeling of the thermal and radiative environment shows that the effect  
 118 of the Radioisotope Thermoelectric Generator (RTG) on TIRS FoV ground heating is  
 119 negligible. This fact has been verified by careful analysis of the ground temperature in  
 120 consideration of the winds, which indicate that the effects are  $< 0.5$  K.

121



122

123 *Figure 1. (a) Diurnal variation of the SEB on sol 30 obtained from MEDA (symbols) and simulated with Single-Column*  
 124 *Models (solid lines – see Methods for further details, and Extended Data Fig. 2, which shows the seasonal evolution of*  
 125 *the daily mean heat flux and related variables). (b) Ground temperature measured by MEDA (black symbols) and*  
 126 *obtained by solving the heat conduction equation for homogeneous terrains (solid red line) using MEDA's net heat flux*  
 127 *(gray symbols in Fig. 1a as the upper boundary condition). The best fit is obtained for  $\text{TI} = 230 \text{ J}\cdot\text{m}^{-2}\cdot\text{K}^{-1}\cdot\text{s}^{-1/2}$ . (c) Footprint*  
 128 *(green shade) of the ground temperature sensor on sol 30. For horizontal terrains as on sol 30, when the rover pitch*

129 *and roll angles were  $-0.25^\circ$  and  $1.29^\circ$ , respectively, this footprint covers an area of a few  $m^2$ . (d) Diurnal evolution of*  
 130 *broadband albedo on sols 125 (blue) and 209 (red). On both sols, the albedo shows a minimum close to noon, with*  
 131 *increasing values towards sunrise and sunset, as the solar zenith angle increases. This non-Lambertian behavior is*  
 132 *similar in other sols, regardless of the type of terrain and geometry of the rover. (e-f) As in Fig. 1c, but for sols 125 and*  
 133 *209.*

134

## 135 **Near-surface thermal profile**

136

137 Another novelty enabled by MEDA is the simultaneous tracking of temperatures at four  
 138 heights: surface, 0.85 m, 1.45 m, and about 40 m, around-the-clock (Fig. 2a). The  
 139 variation of these temperatures along a sol reflects the four main regimes of the ASL:  
 140 (1) daytime convection, (2) an evening transition where the convective boundary layer  
 141 collapses, (3) a nighttime steady regime, and (4) a morning transition where the  
 142 inversion fades and a convective boundary layer grows. Fig. 2b-d show an example of  
 143 the daily evolution of the thermal gradient. Daytime convection peaks at noon with  
 144  $(dT/dZ)_{\max} \approx -35 \text{ K}\cdot\text{m}^{-1}$ , while nighttime stable stratification peaks at 20:00 with  
 145  $(dT/dZ)_{\max} \approx +8 \text{ K}\cdot\text{m}^{-1}$  in the first meter from the surface, reaching values well above the  
 146 adiabatic gradient  $g/C_p = 0.0045 \text{ K}\cdot\text{m}^{-1}$ . Fig 2e shows the seasonal evolution of mean  
 147 temperatures, where the daily average thermal gradient is dominated by the diurnal  
 148 convective period. In most sols, nighttime thermal stability weakens as the night  
 149 progresses, and unstable conditions often develop from 02:00 onward.

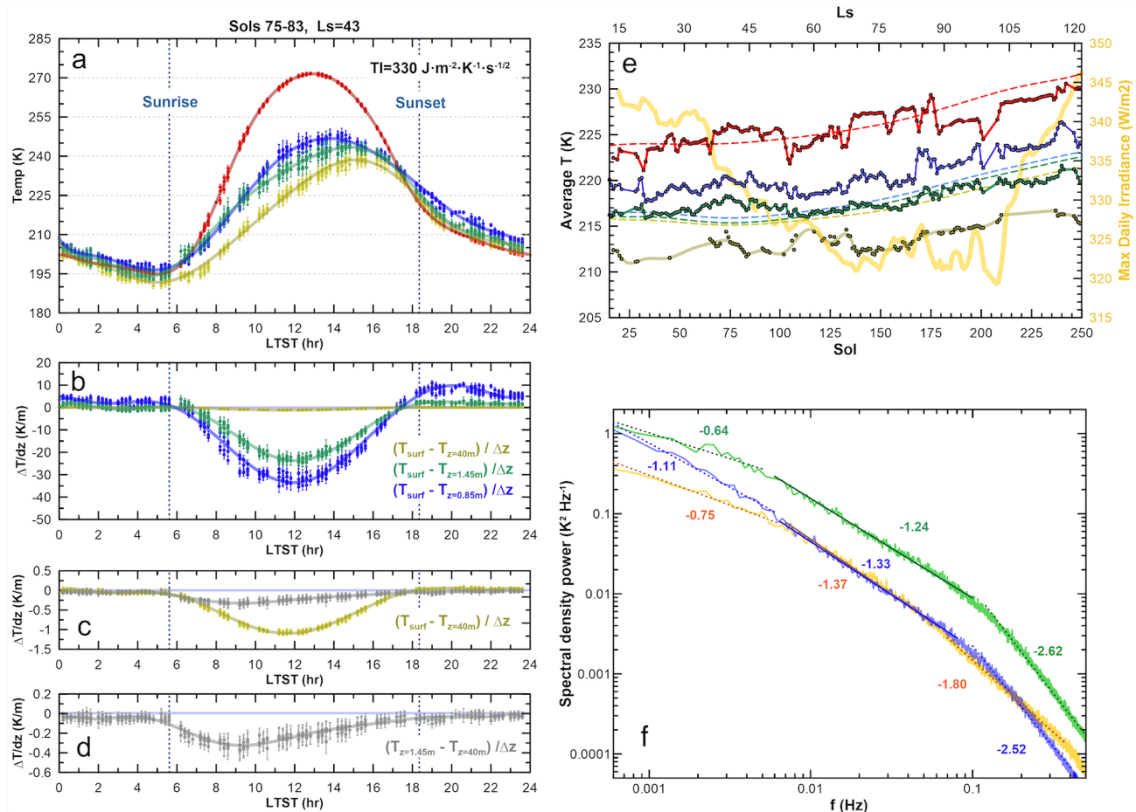
150

151 A similar observation was reported for InSight [14] and attributed to the radiative  
 152 influence of the hardware. Additionally, Curiosity's REMS instrument, measuring on the  
 153 deeper Gale crater, has only seen this inversion broken during the global dust storm  
 154 [15]. However, with MEDA we observe that the characteristics of the nighttime inversion  
 155 breakup depend on local terrain properties, being that TI and the air and surface  
 156 temperatures measured by TIRS are very local and away from rover disturbances (Fig.  
 157 1d). On the other hand, we also observe that the air temperatures at different levels are  
 158 not so sensitive to the specific terrain, decoupling progressively from 0.85 m to 40 m  
 159 (Fig. 2e and Extended Data Fig. 3). Winds driven by horizontal gradients of terrain  
 160 properties may be the origin of the discrepancies we observe, in absolute terms, of the  
 161 measurements with respect to the predictions offered by one-dimensional radiative  
 162 equilibrium models, which typically neglect the role of horizontal winds, although daily  
 163 averages and their trends are in line with such predictions.

164

165 Temperature fluctuations are common throughout the sol: these rise after sunrise  
 166 peaking near noon (amplitudes  $\Delta T_{\max} \sim 10 \text{ K}$ ) and convective in nature, subside before  
 167 sunset, and increase again during the breakup of the nighttime inversion, suggesting  
 168 strong nocturnal turbulence (Extended Data Fig. 4). The nature of these oscillations can  
 169 be investigated by analyzing the spectral slopes. Fig. 2f shows these slopes during the  
 170 convective period, averaged over 250 sol. The results show typical slopes of turbulence  
 171 in daytime hours, with changes at other times of the sol; these will be analyzed in later  
 172 works. MEDA enables the identification of different dynamical regimes, forced, inertial  
 173 and dissipative, more clearly than with previous instruments [16-17] and at different  
 174 altitudes.

175



176  
177  
178  
179  
180  
181  
182  
183  
184  
185  
186  
187  
188  
189  
190  
191

Figure 2. Daily Cycle of temperatures at Jezero under typical values of the TI of the local terrain ( $TI = 330 \text{ J}\cdot\text{m}^{-2}\cdot\text{K}^{-1}\cdot\text{s}^{-1/2}$  in this group of sols as measured by TIRS). Dots corresponds to averages over a time window of 12 minutes. (a) Surface temperatures (red), at  $z = 0.85 \text{ m}$  (blue),  $z = 1.45 \text{ m}$  (green) and  $z \sim 40 \text{ m}$  (green yellow). (b) Thermal gradients from the surface to the near surface at  $0.85 \text{ m}$  (blue) and  $1.45 \text{ m}$  (green). (c) Thermal gradient from the surface to the  $40 \text{ m}$  level (green yellow) and from  $1.45 \text{ m}$  to  $40 \text{ m}$  (grey). (d) Same as (c) but only from  $z = 1.45 \text{ m}$  to  $z = 40 \text{ m}$ . Sunrise and sunset are shown with vertical dotted lines. The adiabatic thermal gradient is shown in plots (b) to (d) with an horizontal light blue line. (e) Seasonal evolution of mean daily air temperatures at Jezero. MEDA TIRS and ATS temperatures (solid lines) at the surface (red),  $z = 0.85 \text{ m}$  (blue),  $z = 1.45 \text{ m}$  (green) and  $z = 40 \text{ m}$  (green yellow) are compared with predictions from the Mars Climate Database [18] (dashed lines). Dots represent measurements using data for 2 consecutive sols to build a full thermal cycle. Long segments, in TIRS data at  $z = 40 \text{ m}$ , correspond to series of sols where clean measurements over a complete thermal cycle were not possible over 2 sols. Yellow line (right axis) shows the maximum irradiance measured by the Radiation and Dust Sensor (RDS) Top 7 sensor and computed for sets of 2 consecutive sols. (f) Statistical analysis of power spectra of temperature fluctuations at  $0.85 \text{ m}$  (blue),  $1.45 \text{ m}$  (green) and  $40 \text{ m}$  (yellow), measured between 10:00 and 15:00 h. Dashed and solid lines show the fit to the data in each frequency range. Figures correspond to the exponential indices of these fits in each frequency range.

192

193

## Pressure fluctuations

194

195

196

197

198

199

200

201

202

203

204

205

206

Turbulence is also present in pressure and horizontal wind measurements. Fig. 3a shows examples of the daily pressure cycle on different sols; this cycle has the contribution of different dynamic phenomena, as discussed below. Analysis of the rapid pressure fluctuations shows a power spectrum similar to that of temperature (Fig. 3b), different from that expected from Kolmogorov turbulence, but similar to that measured by InSight [14]. During the stable nighttime period, the pressure fluctuations are at the detector noise level.

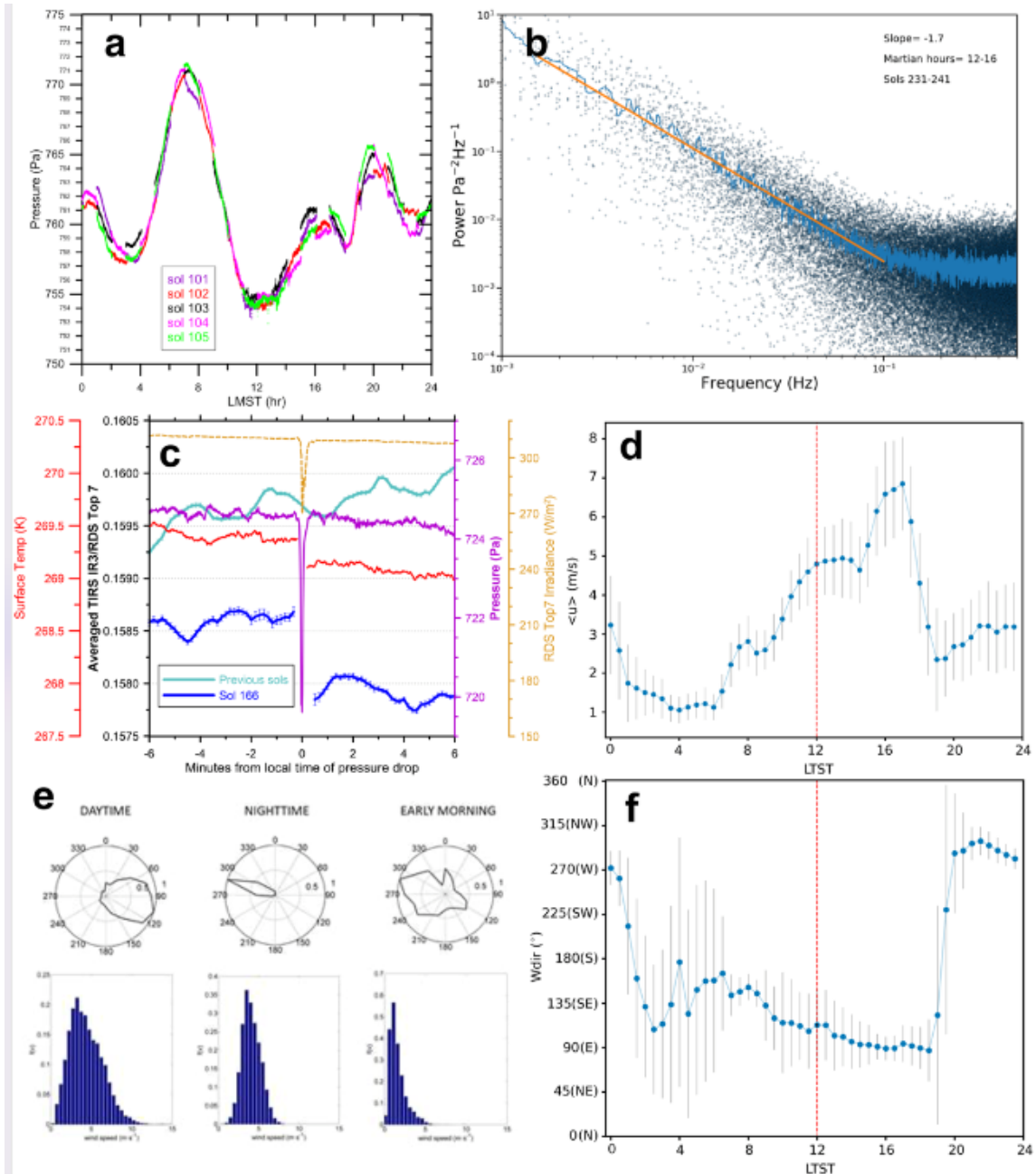
Convection generates transient events detectable through several MEDA sensors, especially in temperature and pressure data (Extended Data Fig. 5). Some events are Dust Devils (DDs), also detected as slight drops ( $\sim 0.4\text{-}26\%$ ) in radiation sensor readings or imaged with Perseverance cameras [19]. Jezero exhibits the highest abundance of

207 DDs so far detected by a mission on the surface of Mars [20]. The pressure drops  
208 detected in this period range from  $\sim 0.3$  to  $6.5$  Pa in intensity, and last from 1 to 200 s.  
209 DDs where simultaneous wind data is available have estimated diameters from 5 to 500  
210 m, with vortices having rotational speeds of  $\sim 3$  to  $30$   $\text{m}\cdot\text{s}^{-1}$ . A small number of these  
211 produced measurable albedo changes on the surface as they remove dust (Fig. 3c).

212

213 Winds show a daily cycle with maximum values of  $7$   $\text{m}\cdot\text{s}^{-1}$  in the afternoon, and near null  
214 between 04:00 and 06:00 (Fig 3d). Strong gusts are detected with maximum speeds of  
215  $25$   $\text{m}\cdot\text{s}^{-1}$  at midday. Turbulence creates fluctuating winds of about  $2$ - $4$   $\text{m}\cdot\text{s}^{-1}$  at night,  
216 where they are likely responses to horizontal shear flows, and  $5$ - $7$   $\text{m}\cdot\text{s}^{-1}$  during the  
217 convective hours (Fig. 3e). Pre-landing atmospheric modeling predicted that diurnal  
218 upflows and nocturnal downflows on the Isidis basin slopes would dominate the overall  
219 wind pattern, with Jezero local topography causing a relatively small but measurable  
220 effect [12-13]. Wind data support the dominance of diurnal upslope currents from  
221 roughly south-east, with a reversal of winds at night [13] (Fig. 3e-f). These diurnal wind  
222 patterns drive aeolian erosion at Jezero [20] and show a variety of behaviors resulting  
223 from a complex interaction between regional circulation, slope winds, and interaction  
224 with the general circulation and the large scale Hadley cell flow.

225



226  
 227 *Figure 3. (a) Daily pressure cycles for sols 101 to 105, showing the deviations from the mean values caused by the*  
 228 *contributions of different dynamic phenomena. (b) Power spectrum obtained from the analysis of pressure*  
 229 *fluctuations from sols 231 to 241. The straight line determines the power law fit in the frequency range 0.001 to 0.1*  
 230 *Hz. (c) Dust Devil record observed on sol 166; the pink line reflects the sudden pressure drop caused by the passage of*  
 231 *the convective vortex, while the blue line shows the jump caused in the radiation ratio measured by TIRS and RDS,*  
 232 *versus the same magnitude on preceding sols (cyan line). (d) Mean values every 30 min in horizontal wind speed, with*  
 233 *the corresponding mean deviation for each period, averaged over 250 sols. The difference in behavior and fluctuations*  
 234 *in daytime and nighttime hours, as a consequence of the different regimes, can be seen. (e) Wind rose diagrams and*  
 235 *histograms of wind flows in different time slots. It is observed the dominance of descending winds during the night*  
 236 *and ascending winds during the day, with the change of tendency in the early hours of the day. (f) Record of wind*  
 237 *directions for a typical sol.*

238

## 239 Atmospheric dust properties

240

241 For the first time, SkyCam is tracking the regular morning-evening opacity cycle in the  
 242 visual range (550 nm) as a function of time (Fig. 4a). During the clear season covered by

243 this study, persistently higher opacity is observed in the morning (optical depth, OD,  
244  $\sim 0.5$ ) than in the afternoon (OD  $\sim 0.4$ ). Analysis of RDS data at different wavelengths and  
245 observation geometry allows to determine the optical properties of the dust, and to  
246 derive the OD variation at high temporal resolution (Fig. 4b). The dust optical properties  
247 and OD are estimated by comparing the temporal variation of the measured sky spectral  
248 intensity, with radiative transfer simulations (Fig. 4c shows an example). Most of the  
249 particle-size information is obtained when the Sun trajectory is near one of the RDS  
250 lateral-sensors FoV. From these observations we found particle sizes ranging from  $\sim 1.2$   
251 to  $1.4 \mu\text{m}$ , consistent with previous studies. To estimate the non-sphericity of those  
252 particles, the T-matrix approach was used to compute the phase function, single  
253 scattering albedo and the extension cross section.

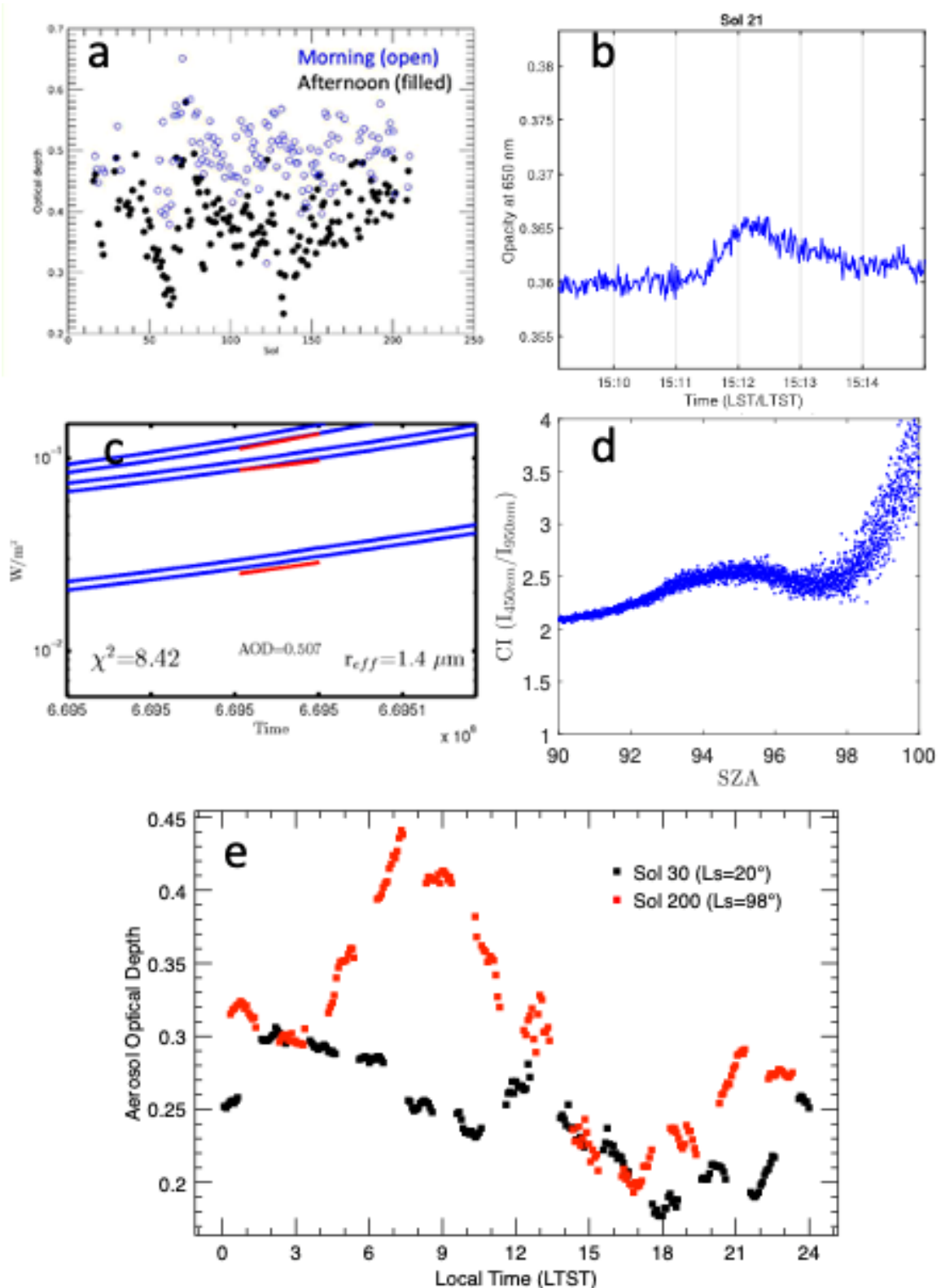
254

255 This phase of the mission fell within the aphelion cloud belt season, and near the peak  
256 latitude for water ice clouds [21]. It is therefore likely that some of the afternoon opacity  
257 in Fig. 4a, including the increase around sol 70 and most of the morning-afternoon  
258 difference, is due to water ice hazes. Clouds were observed around sol 70 and 180, but  
259 discrete clouds were not typically present during daytime [19]. During this season, a low  
260 dust OD (0.3-0.6), with low variability, is typical of other sites [22-23]. We have also  
261 found cloud signatures during daytime and twilight. In the latter cases (Fig. 4d)[24], we  
262 could constrain the cloud altitudes using radiative transfer simulations. In most cases,  
263 we found cloud altitudes around or above 40 km, and particle sizes larger than  $1 \mu\text{m}$   
264 (indicative of water ice particles).

265

266 The daily OD evolution was also retrieved from TIRS infrared measurements,  
267 strengthening the case for nighttime clouds. Fig. 4e shows the diurnal variation of  
268 thermal-IR aerosol OD, contributed by both dust and water ice clouds, as a function of  
269 local time for two representative sols. Because TIRS observes thermal-IR radiation, this  
270 retrieval is possible for all local times including during the night, a capability not available  
271 on previous rovers except by Mini-TES on-board MER rovers, which could only make  
272 limited and occasional nighttime observations [25]. The OD observed by TIRS during sol  
273 30 ( $L_s=20^\circ$ ) shows a moderate variation with greater opacity at night than during the  
274 day. By sol 200, the aphelion season cloud belt [26] was near its peak annual amplitude,  
275 and data reveal a significant diurnal variation in OD with maximum clouds shortly after  
276 dawn. This ability to track OD throughout each sol is a powerful tool that leads to new  
277 insights about how dust and water ice clouds interact with the surface and the rest of  
278 the atmosphere.

279



280  
 281 *Figure 4. (a) OD derived from images taken regularly by SkyCam to follow the day-night cycle in the visual range (550*  
 282 *nm). A regular pattern of higher values in the morning hours than in the afternoon is observed, consistent with*  
 283 *measurements made more occasionally with MastCam-Z [19]. (b) Analysis of the RDS photodiode observations also*  
 284 *allows the derivation of the OD at a temporal resolution of 1 second, and thus determine the variations produced by*  
 285 *short-duration events such as dust devils. (c) Example of dust particle radius and OD estimation using RDS observations*  
 286 *at different wavelengths, and radiative transfer simulations. The best fit between observations and simulations is*  
 287 *obtained for an effective radius  $r_{eff} = 1.4 \mu\text{m}$ . (d) Variation of the color index (CI), defined as the ratio of the RDS*  
 288 *observations at zenith at 450 and 950 nm, to the solar zenith angle (SZA) measured on sol 296. The SZA of maximum*  
 289 *CI indicates that this cloud layer is found at altitudes above 45 km. (e) The aerosol OD at  $9 \mu\text{m}$  retrieved from TIRS*

290 *upward-looking observations for sols 30 (Ls=20°) and 200 (Ls=98°) as a function of local time (LTST). TIRS observations*  
291 *enable aerosol OD to be retrieved at all local times. The large diurnal variation for sol 200 is likely caused by water ice*  
292 *clouds.*

293

## 294 **A complex humidity cycle**

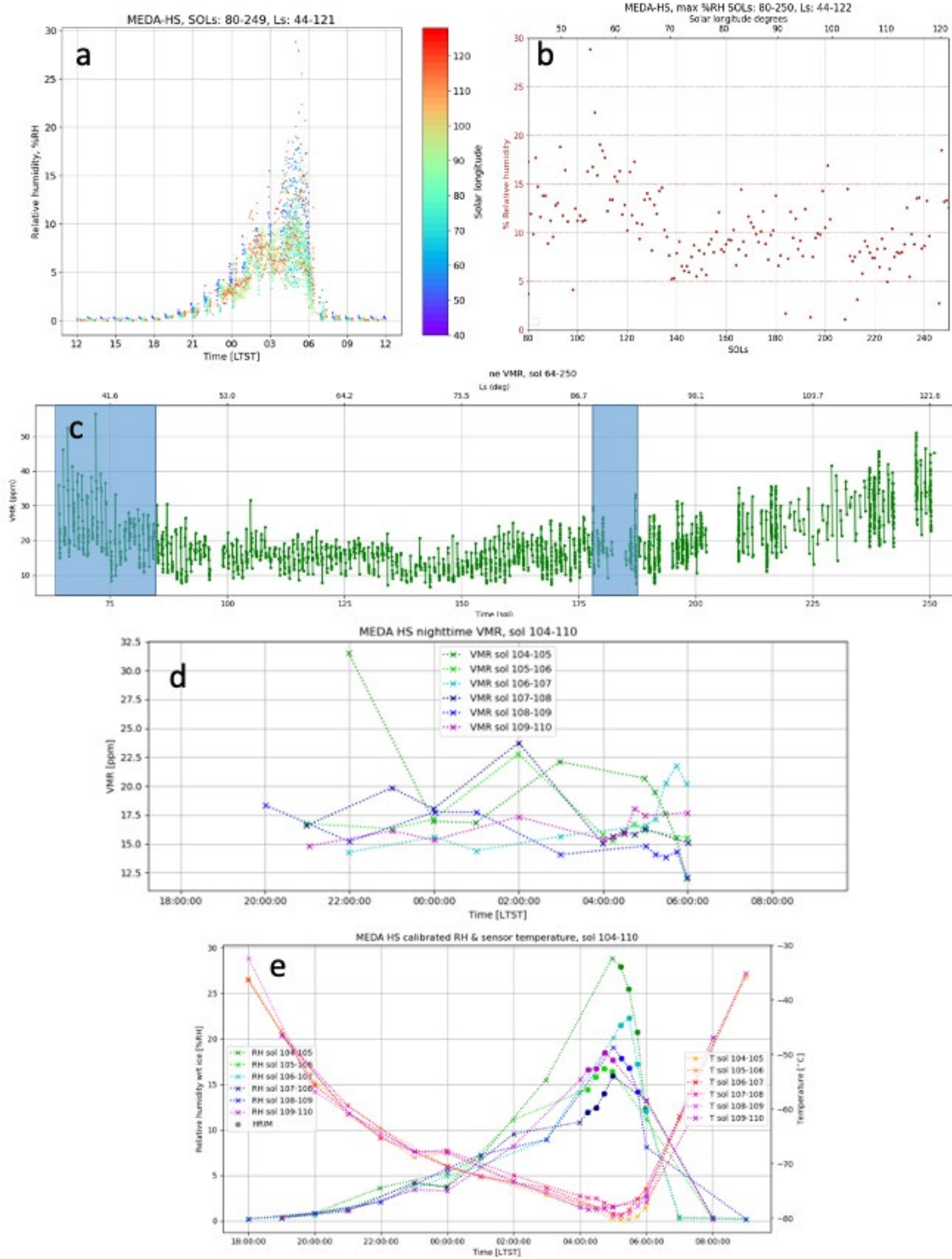
295

296 Measuring the relative humidity (RH) in the ASL on diurnal and seasonal time scales is a  
297 key element in understanding hydrological processes in the Martian atmosphere.  
298 MEDA's humidity sensor (HS) often finds a nocturnal hydrological cycle more complex  
299 than anticipated in numerical predictions [12]. Fig. 5a shows the daily and seasonal  
300 behavior of RH, while Fig. 5b shows the daily maxima recorded in the period studied.  
301 Likewise, Fig. 5c shows the seasonal variations of nighttime water vapor Volume Mixing  
302 Ratio, VMR. Within the diurnal cycle, the maximum, typically in the range 15-30% in RH  
303 (referred to HS temperature), occurs in the early morning, with maximum VMR being  
304 reached around midnight. Nocturnal water vapor amounts at Jezero during the seasons  
305 are lower than those at Gale and models predictions [12].

306

307 MEDA measured a seasonal minimum in nighttime VMR near Ls=70, with higher  
308 abundance and greater variability at the end of the season (Fig. 5c). Additionally, a large  
309 increase in VMR was observed on the evening of sol 104 (Fig. 5d-e), accompanied by  
310 cooling atmospheric temperatures. The increase in RH slowly returned to typical values,  
311 while the temperature continued dropping. This behavior may be due to a single dry air  
312 mass advected over the rover bringing cold, dry air, which then remains in the area. An  
313 alternative is that it is related to the local surface and possible exchange processes. In  
314 the early morning of sol 105, frost conditions were possible as seen by comparing the  
315 calculated frost point (at 1.45 m) to the TIRS ground temperature. A resulting  
316 hypothesis is that, if sub-surface exchange is occurring, the actual frost point at the  
317 atmosphere-surface interface may be lower owing to less vapor present in the  
318 atmosphere.

319



320  
 321 *Figure 5. (a) Daily and seasonal evolution of RH, with the temporal resolution provided by MEDA HS. (b) Seasonal*  
 322 *evolution of the maximum RH values observed in the study period, reaching an absolute maximum of 29% RH,*  
 323 *referring to the temperature recorded by the sensor included in the HS itself. (c) Seasonal behavior of the VMR, where*  
 324 *it is observed that the maximum reached 37 ppm, compared to the 300 ppm predicted by the models for this season*  
 325 *[12]. (d) Detail of the daily evolution of characteristic sols, where the complex and temporally variable structure of*  
 326 *the nocturnal hydrological cycle can be observed, sometimes not foreseen by the simulation models. Also shown are*  
 327 *the temperatures recorded by the HS itself, with respect to which the RH is estimated. (e) Daily evolution of the VMR*  
 328 *for the same sols shown in figure (d) of this panel.*

329

330

## 331 **Non-local dynamical phenomena**

332

333 The daily pressure cycles at Jezero showed a rich variability, reflecting the action of  
334 different dynamical mechanisms in the atmosphere under a variety of spatial and  
335 temporal scales (Fig. 3a). On the seasonal scale, as the Northern Polar cap sublimated,  
336 the daily mean pressure increased from 735 Pa on sols 15-20 ( $L_s=13^\circ-16^\circ$ ) to a maximum  
337 of 761 Pa on sols 99-110 ( $L_s=52^\circ-57^\circ$ ). It then gradually decreased to 650 Pa in sol 250  
338 ( $L_s=125^\circ$ ) as the Southern polar cap grows (Fig. 6a).

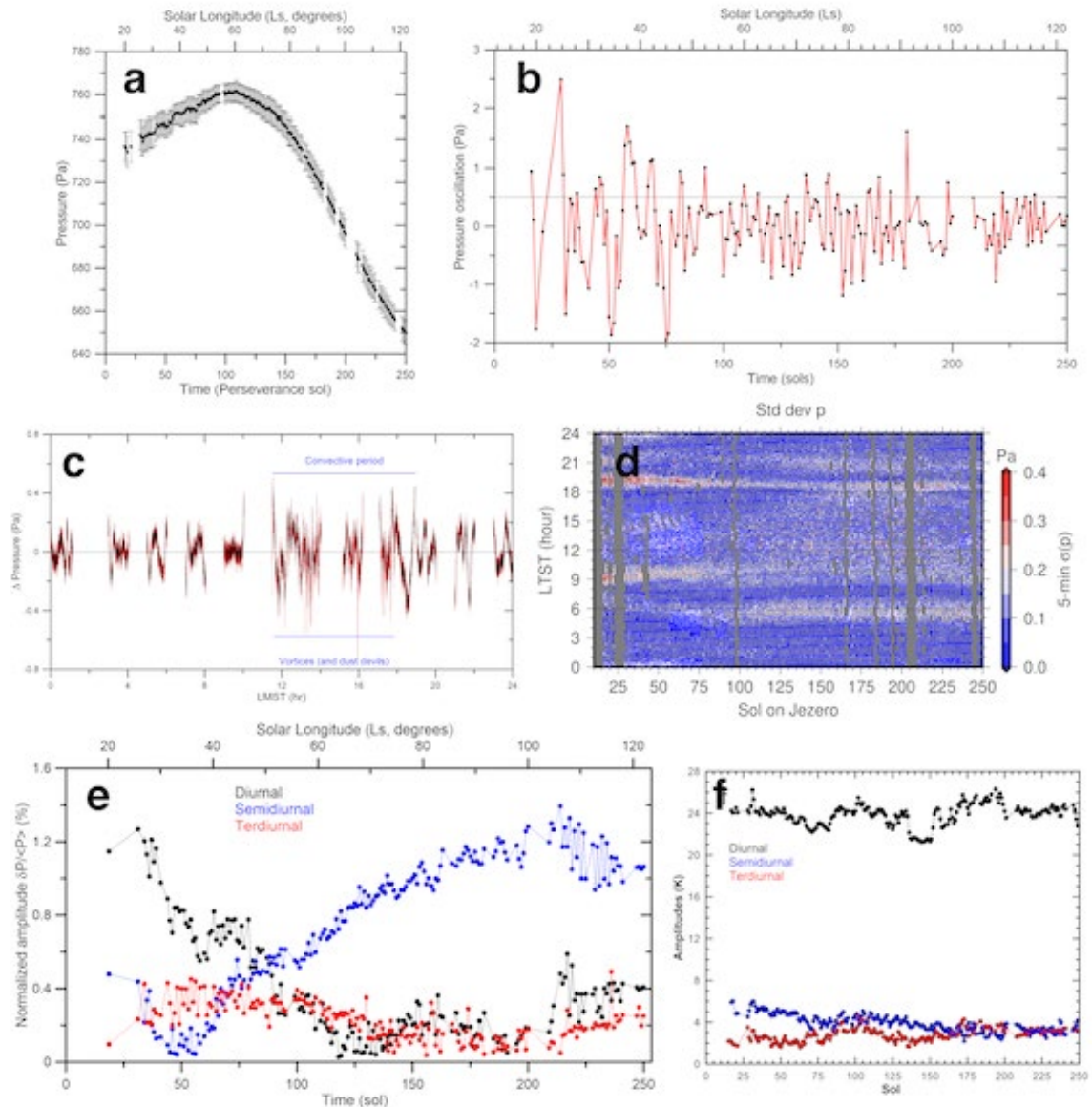
339

340 The residuals resulting from the difference between the mean daily pressure and a  
341 polynomial fit to the data show oscillating behavior with a mean period of about 4.5  
342 sols; when superimposed, other oscillations with longer periods are observed (Fig. 6b).  
343 This is the signature of what could be high-frequency travelling waves arising from  
344 baroclinic instabilities also reported in other sites [6]. More sols and joint analysis of  
345 satellite data will be needed to confirm this fact. Additionally, the residuals resulting  
346 from a fit to the approximately 1-hour measurement series (Fig. 6c) show regular  
347 oscillations that, on average, have a peak-to-peak amplitude of 0.2-0.4 Pa and periods  
348 between 12 and 20 minutes. These oscillations are due to the passage of gravity waves,  
349 also observed elsewhere on Mars [27]. Fig. 6d shows the seasonal and diurnal pressure  
350 variability, where the daily patterns of pressure changes are observed.

351

352 Thermal tides cause the large modulation of the daily pressure cycle. A Fourier analysis  
353 of that cycle shows that up to six components are present, with maximum amplitudes  
354 ranging from 0.2 to 10 Pa. Fig 6e shows the wide variability of the normalized amplitude  
355 of diurnal and semidiurnal tides. The maximum relative change observed in the studied  
356 period is  $(\delta P / \langle P \rangle)_{\max} \sim 0.013$ . Smaller changes also occurred in tidal components 3 and 4.  
357 The semi-diurnal component showed a very strong drop between sols 20 and 50;  
358 although still under investigation, it may suggest a relation to the dust loading present  
359 on those sols, or the development of disturbances at the polar cap edge. Tides are also  
360 detected in the Fourier analysis of the temperature data with half-amplitudes of 26 K  
361 (diurnal), 2-6 K (semidiurnal) and 2-4 K (terdiurnal), as shown in Fig. 6f. The tidal  
362 variability is mainly related to changes in atmospheric opacity produced by clouds and  
363 dust loading at different altitudes [19]. The period studied is the non-dusty season on  
364 Mars, which makes the variability relatively low.

365



366  
 367 *Figure 6. (a) Seasonal variation of daily mean pressure values, and their corresponding daily ranges. (b) Oscillations*  
 368 *obtained in the differences between the daily mean values and the polynomial fit of the measurements, where 2*  
 369 *intervals are clearly observed, before and after the sol ~80. (c) Oscillations obtained in the infra-daily differences. (d)*  
 370 *Detrended standard deviation of pressure, as a function of sol and LTST, after subtracting least squares fit of the*  
 371 *observed pressure. Removing the tidal components shows that the dominant contribution to pressure variability*  
 372 *occurs during the hours with strong convection and after a calm period. The figure shows the trend changes between*  
 373 *05:00-07:00, and 17:00-19:00. (e) First 3 components of the Fourier analysis of the pressure cycle: diurnal (24-hour*  
 374 *period –black–), semidiurnal (12-hour periods –blue–) and terdiurnal (6-hour period –red–) components. (f) Equivalent*  
 375 *Fourier analysis of the temperature data at  $z = 1.45$  m: diurnal (blue) and semidiurnal (red) components.*

376

377 **Discussion**

378

379 M2020 includes a payload to monitor an environment that exhibits a rich diversity of  
 380 behaviors. Many of the measurements made by MEDA so far are the first time they have  
 381 been obtained on Mars, revealing interesting surprises in Jezero's atmosphere.

382

383 The SEB is measured for the first time in situ. The design of future engineering systems,  
 384 the understanding and modeling of photochemical reactions at the surface, or the

385 interpretation of satellite measurements benefit from these results. An example is the  
386 characterization of the non-Lambertian reflection of the surface that must be  
387 considered in the interpretation of orbital observations of variations in albedo, when  
388 trying to understand changes in the physical properties of the surface.

389

390 Globally, the measured daily temperature cycle agrees with model predictions (although  
391 with some deviations in the vertical temperature gradient), expected magnitude of  
392 thermal oscillations, and the seasonal evolution. Also, the observed vortex convective  
393 activity matches the predictions of Large-Eddy-Simulation (LES) using the MarsWRF  
394 model [20]. However, when analyzing vertical temperature profiles, we find a diversity  
395 of nocturnal responses that raise intriguing questions about what is happening at the  
396 different locations traversed by the rover.

397

398 Several independent radiation sensors and methods have measured the occurrence and  
399 even development of nighttime clouds, long before the peak of the cloud season. The  
400 ability to track OD throughout each sol is a powerful tool that has shown the prevalence  
401 of clouds near dawn, and will lead to new insights about how dust and water ice clouds  
402 interact with the surface and the rest of the atmosphere.

403

404 The observed nocturnal hydrologic cycle is more complex than anticipated by the  
405 models and is also observed in Gale. This unpredicted behavior can be due to a variety  
406 of causes, yet to be explored in detail.

407

408 Thermal tides show smaller pressure amplitudes at Jezero when compared with  
409 Curiosity's observations [28] or Viking [29]. While the general behavior at Jezero was  
410 predicted by the models [12-13], there are differences in its amplitude and timing likely  
411 due to the interaction of local topography with the air masses exchanges between the  
412 interior and exterior of the basin. Another interesting result is the existence of multisol  
413 waves at a time of the season when baroclinic waves have been observed to have very  
414 limited activity.

415

416 Overall, MEDA observations show a dynamic environment rich in atmospheric  
417 phenomena that is different from other locations on Mars studied by previous missions.  
418 The characterization of Jezero's atmosphere plays an important role in the development  
419 of the Mars Sample Return mission, and in the exposure of the samples being collected  
420 by Perseverance.

421

422

423

424

425

426

427

428

429

430

431

432

433 **References**

434

435 1. Farley, K.A. et al. (2020) Mars 2020 Mission Overview. *Space Sci. Rev.*, 216:142. doi:  
436 10.1007/s11214-020-00762-y.

437

438 2. Rodriguez-Manfredi J. A. et al. (2021) The Mars Environmental Dynamics Analyzer,  
439 MEDA. A Suite of Environmental Sensors for the Mars 2020 Mission. *Space Sci. Rev.*,  
440 217.3, 1-86. doi: 10.1007/s11214-021-00816-9.

441

442 3. Hess, S.L., Henry, R.M., Leovy, C.B., Ryan, J.A. and Tillman, J.E. (1997) Meteorological  
443 results from the surface of Mars: Viking 1 and 2, *Journal of Geophysical Research*, 82  
444 (28), 4559-4574.

445

446 4. Schofield, J. T., Barnes, J.R., Crisp, D., Haberle, R.M., Larsen, S., Magalhaes, J.A.,  
447 Murphy, J.R., Seiff, A. and Wilson, G. (1997) The Mars Pathfinder atmospheric structure  
448 investigation/meteorology (ASI/MET) experiment, *Science*, 278, 1752–1758,  
449 doi:10.1126/science.278.5344.1752.

450

451 5. Taylor, P.A., Catling, D.C., Daly, M., Dickinson, C.S., Gunnlaugsson, H.O., Harri, A.-M.  
452 and Lange, F. (2008) Temperature, pressure and wind instrumentation on the Phoenix  
453 meteorological package, *J. Geophys. Res.*, 113, EA0A10, doi:10.1029/2007JE003015.

454

455 6. Smith, M.D., Wolff, M.J., Lemmon, M.T., Spanovich, N., Banfield, D., Budney, C.J.,  
456 Clancy, R.T., Ghosh, A., Landis, G.A., Smith, P.H. and Whitney, B. (2004) First atmospheric  
457 science results from the Mars Exploration Rovers Mini-TES. *Science*, 306 (5702), 1750-  
458 1753.

459

460 7. Gómez-Elvira, J., Armiens, C., Castañer, L., Domínguez, M., Genzer, M., Gómez, F.,  
461 Haberle, R.M., Harri, A.-M., Jiménez, V., Kahanpää, H., Kowalski, L., Lepinette, A., Martín,  
462 J., Martínez-Frías, J., McEwan, I., Mora, L., Moreno, J., Navarro, S., de Pablo, M.A.,  
463 Peinado, V., Peña, A., Polkko, J., Ramos, M., Renno, N.O., Ricart, J., Richardson, M.,  
464 Rodríguez-Manfredi, J.A., Romeral, J., Sebastián, E., Serrano, J., de la Torre Juárez, M.,  
465 Torres, J., Torrero, F., Urquí, R., Vázquez, L., Velasco, T., Verdasca, J., Zorzano, M.-P., and  
466 Martín-Torres, J. (2012) REMS: The Environmental Sensor Suite for the Mars Science  
467 Laboratory Rover. *Space Science Review*, 170:583–640, doi:10.1007/s11214-012-9921-  
468 1.

469

470 8. Banfield, D., Rodriguez-Manfredi, J.A., Russell, C.T., Rowe, K.M., Leneman, D., Lai,  
471 H.R., Cruce, P.R., Means, J.D., Johnson, C.L., Mittelholz, A., Joy, S.P., Chi, P.J., Mikellides,  
472 I.G., Carpenter, S., Navarro, S., Sebastian, E., Gomez-Elvira, J., Torres, J., Mora, L.,  
473 Peinado, V., Lepinette, A., the TWINS Team, Hurst, K., Lognonné, P., Smrekar, S.E.,  
474 Banerdt, W.B. (2019) InSight Auxiliary Payload Sensor Suite (APSS). *Space Science  
475 Review*, 215 :4, doi: 10.1007/s11214-018-0570-x.

476

477 9. Read PL, Lewis SR, Mulholland DP (2015) The physics of Martian weather and climate:  
478 a review. *Rep Prog Phys*. 78(12):125901. doi: 10.1088/0034-4885/78/12/125901

- 479  
480 10. Martínez, G. M., Vicente-Retortillo, A., Vasavada, A. R., Newman, C. E., Fischer, E.,  
481 Rennó, N. O. and Sánchez-Lavega, A. (2021) The surface energy budget at Gale crater  
482 during the first 2500 sols of the Mars Science Laboratory mission. *Journal of Geophysical*  
483 *Research: Planets*, 126(9), doi: e2020JE006804.
- 484  
485 11. Vicente-Retortillo, Á., Valero, F., Vázquez, L. and Martínez, G. M. (2015) A model to  
486 calculate solar radiation fluxes on the Martian surface. *Journal of Space Weather and*  
487 *Space Climate*, 5, A33.
- 488  
489 12. Pla-García, J., Rafkin, S.C.R., Martinez, G.M., Vicente-Retortillo, A., Newman, C.E.,  
490 Savijärvi, H., de la Torre, M., Rodriguez-Manfredi, J.A., Gomez, F., Molina, A., Viudez-  
491 Moreiras, D., Harri, A.-M. (2020) Meteorological predictions for Mars 2020 Perseverance  
492 Rover landing site at Jezero Crater. *Space Sci. Rev.*, 216:148.
- 493  
494 13. Newman et al. (2021) Multi-model meteorological and aeolian predictions for Mars  
495 2020 and the Jezero Crater region. *Space Sci. Rev.*, 217:20.
- 496  
497 14. Banfield et al. (2020) The atmosphere of Mars as observed by InSight. *Nat. Geo*, 13,  
498 190-198. doi: 10.1038/s41561-020-0534-0.
- 499  
500 15. Guzewich et al. (2019) Mars Science Laboratory observations of the 2018/Mars year  
501 34 global dust storm. *Geophys. Res. Lett.* 46(1). doi: 10.1029/2018GL080839.
- 502  
503 16. Larsen, S.E., Jørgensen, H.E., Landberg, L., Tillman, J.E. (2002) Aspects of the  
504 atmospheric surface layers on Mars and Earth, *Boundary Layer Meteorol.*, 105, 451–  
505 470, doi: 10.1023/A:1020338016753.
- 506  
507 17. Davy, R., Davis, J.A., Taylor, P.A., Lange, C.F., Weng, W., Whiteway, J. and  
508 Gunnlaugson, H.P. (2010) Initial analysis of air temperature and related data from the  
509 Phoenix MET station and their use in estimating turbulent heat fluxes, *J. Geophys. Res.*,  
510 115, E00E13, doi:10.1029/2009JE003444.
- 511  
512 18. Millour, E., Forget, F., et al. (2015) The Mars Climate Database (MCD version 5.2).  
513 European Planetary Science Congress 2015.
- 514  
515 19 Bell, *Sci. Adv.* (2022, submitted)
- 516  
517 20. Newman, *Sci. Adv.* (2022, submitted)
- 518  
519 21. Wolff, J.M., Clancy, R.T., Kahre, M.A., Haberle, R.M., Forget, F., Cantor, B.A., Malin,  
520 M.C. (2019) Mapping water ice clouds on Mars with MRO/MARCI. *Icarus*, 332, pp. 24-  
521 49.
- 522  
523 22. Lemmon et al. (2015) Dust aerosol, clouds, and the atmospheric optical depth record  
524 over 5 Mars years of the Mars Exploration Rover mission. *Icarus*, 251, 96-111, doi:  
525 10.1016/j.icarus.2014.03.029.

526

527 23. Montabone, L., Spiga, A., Kass, D.M., Kleinboehl, A., Forget, F., and Millour, E. (2020)  
528 Martian year 34 column dust climatology from mars climate sounder observations:  
529 Reconstructed maps and model simulations. *Journal of Geophysical Research: Planets*,  
530 123.

531

532 24. Toledo, D., Arruego, I., Apestigue, V., Jimenez, J.J., Gomez, L., Yela, M., Rannou, P.,  
533 Pommereau, J.-P. (2017) Measurement of dust optical depth using the solar irradiance  
534 sensor (SIS) onboard the ExoMars 2016 EDM. *Planetary and Space Science*, 138, pp. 33-  
535 43.

536

537 25. Smith, M.D., Wolff, M.J., Spanovich, N., Ghosh, A., Banfield, D., Christensen, P.R.,  
538 Landis, G.A., Squyres, S.W. (2006) One Martian year of atmospheric observations using  
539 MER Mini-TES. *J. Geophys. Res.*, 111, E12S13, doi: 10.1029/2006JE002770.

540

541 26. Clancy, R.T., Montmessin, F., Benson, J., Daerden, F., Colaprete, A., Wolff, M.J.  
542 (2017) Mars Clouds, Chapter 5 in "The Atmosphere and Climate of Mars". Cambridge  
543 University Press. doi: 10.1017/9781139060172.005.

544

545 27. Guzewich, S.D., de la Torre Juárez, M., Newman, C.E., Mason, E., Smith, M.D., Miller,  
546 N., et al. (2021) Gravity wave observations by the Mars Science Laboratory REMS  
547 pressure sensor and comparison with mesoscale atmospheric modeling with MarsWRF.  
548 *J. Geophys. Res.: Planets*, 126(8), doi: 10.1029/2021je006907.

549

550 28. Haberle et al. (2014) Preliminary interpretation of the REMS pressure data from the  
551 first 100 sols of the MSL mission. *J. Geophys. Res.: Planets*, 119, 440-453, doi:  
552 10.1002/2013JE004488.

553

554 29. Zurek, R.W. (1981) inferences of dust opacities for the 1977 Martian great dust  
555 storms from Viking Lander 1 pressure data. *Icarus*, 45, 202-215.

556

557

558

559

560

561

562

563

564

565

566

567

568

569

570

571

**572 Methods**

573

**574 MEDA operational strategy**

575

576 MEDA can operate continuously and independently of the rover's battery charge cycles,  
577 24 hours a day, and subject to a measurement program sent from Earth (Extended Data  
578 Fig. 1). The observation sessions are subject to power availability and, eventually, to  
579 incompatibility with other activities to be performed by the rover.

580

581 Due to these restrictions, the usual sequence of measurements that MEDA is carrying  
582 out consists of the acquisition of all the magnitudes that the instrument records every  
583 other hour. On the following sol, the measurement hours are reversed, so that every  
584 two sols, a total coverage of all daily magnitudes is made.

585

**586 TIRS measurements and analysis**

587

588 The Thermal IR Sensor (TIRS) is an infrared radiometer with five channels which measure  
589 downward radiation (IR1), air temperature (IR2), reflected shortwave radiation (IR3),  
590 upward longwave radiation (IR4) and ground temperature (IR5). We use the ratio  
591 between TIRS IR3 and the "total light" TOP7 detector of the Radiation and Dust Sensor  
592 (RDS, described below) measurements as a proxy for surface albedo. Since TIRS and RDS  
593 measure in different bands, a correction is made using the COMIMART radiative transfer  
594 model [11].

595

596 TI can be straightforwardly derived across Perseverance's traverse by using MEDA values  
597 of the net heat flux into the ground as the upper boundary condition to solve the heat  
598 conduction equation for homogeneous terrains. This quantity governs the thermal  
599 amplitude in the shallow subsurface from diurnal to seasonal to diurnal timescales, and  
600 therefore accurate estimations of TI can be useful to constrain the thermal environment  
601 of the samples collected by the Mars 2020 mission. For this estimation, numerical  
602 models need to simulate the SEB (see other paragraphs below in this section). MEDA  
603 measures the SEB, allowing for a more in-situ-based estimation of the TI.

604

605 Concerning TIRS IR fluxes, the two upward-viewing sensors of TIRS (IR1 and IR2) enable  
606 the total column optical depth of aerosol above the rover to be retrieved. The observed  
607 signal in TIRS IR1 is sensitive to a combination of atmospheric temperatures and total  
608 aerosol optical depth (dust plus water ice cloud). The atmospheric temperature profile  
609 is taken from concurrent observations by the EMIRS instrument on-board the Emirates  
610 Mars Mission [30] with temperatures near the surface modified to match the observed  
611 TIRS IR2 signal. A radiative transfer model including aerosol scattering is then used to  
612 find the aerosol optical depth that would produce the observed TIRS IR1 signal. The  
613 estimated uncertainty in these retrievals is  $\pm 0.03$ .

614

**615 RDS measurements and analysis**

616

617 The Radiation and Dust Sensor (RDS) comprises two sets of 8 photodiodes (RDS-DP)  
618 and a camera (SkyCam)[31]. One set of photodiodes is pointed upward, with each one  
619 covering a different wavelength range between 190-1200 nm. The other set is pointed  
620 sideways, 20 degrees above the horizon, and they are spaced 45 degrees apart in  
621 azimuth to sample all directions at a single wavelength.

622

### 623 **HS measurements and analysis**

624

625 The Humidity Sensor (HS) provides directly the local relative humidity (RH) and local  
626 sensor temperature. Combined with the pressure data provided by the MEDA Pressure  
627 sensor (PS), water vapor volume mixing ratio (VMR) can be calculated too. The HS has  
628 two measurement modes: continuous measurement and high-resolution interval mode  
629 (HRIM). In HRIM the HS is powered on only for 10 seconds and then powered off to avoid  
630 self-heating. HRIM provides the measurements with the best accuracy but continuous  
631 measurements are beneficial for monitoring changes in RH during short time periods.

632

### 633 **PS measurements and analysis**

634

635 The pressure sensor (PS) is actually a set of 2 capacitive transducers that provide the  
636 hydrostatic pressure as a function of the local temperature, for which the sensor also  
637 provides its own temperature [2].

638

639 They are the Barocaps<sup>®</sup> RSP2M and NGM (due to the internal operation of the sensor,  
640 only one or the other can work, not both simultaneously), which can be operated at 0.5  
641 or 1 Hz; the first one has a worse resolution and worse stability than the second one,  
642 but its warm-up time is shorter.

643

### 644 **ATS measurements and analysis**

645

646 Atmospheric Temperature Sensors (ATS) are thin thermocouple sensors with 3 sensors  
647 distributed azimuthally around the Remote Sensing Mast (RSM) at an altitude of 1.45 m,  
648 and 2 sensors on the front sides of the rover at an altitude of 0.85 m, which can provide  
649 local temperature measurements at a configurable rate. The location of 3 sensors  
650 around the RSM ensures that at least one of them is located downwind during most of  
651 the time producing a clean measurement of air temperature. The 2 sensors at 0.85 m  
652 are more shielded from the environment.

653

654 A systematic comparison of ATS data and winds measurements, including the rover  
655 orientation on each individual sol, guided us to use the following rules to select the  
656 appropriate ATS to characterize the unperturbed atmosphere. During diurnal hours the  
657 sensor at  $z = 1.45$  m measuring the lowest temperature is generally the one located  
658 downwind. In certain wind conditions, 2 sensors can be located downwind, and they  
659 show very similar temperatures (within 0.1 K) and equivalent oscillations. At  $z = 0.85$  m  
660 during diurnal hours we select the sensor with the lowest temperature. To take into  
661 account changes in wind direction that modify the selected ATS we consider slow  
662 transitions from one sensor to other at each level when the sensor measuring the lowest  
663 temperature changes. During nighttime, the smaller values of the winds and the

664 sheltered location of the two ATS at  $z = 0.85$  m typically result in one sensor generally  
665 much warmer than the other. Comparison with environment winds indicate that the  
666 lowest temperature sensor is always the most exposed to environment winds with the  
667 lowest thermal perturbations from the rover. In the RSM all 3 ATS can experience  
668 radiative cooling effects from the rover deck. Thus, when two ATS have highly correlated  
669 values and thermal oscillations, we use the average of them instead of the ATS with the  
670 lowest temperature. Thermal perturbations from the Radioisotope Thermal Generator  
671 (RTG) are easily observed at night at  $z = 1.45$  m and identified from the wind data and  
672 rover orientation and do not play any significant effect in the results here presented.  
673 The RTG, located at the back of the rover, does not generally cause detections in the  
674 sheltered detectors in the front of the rover at  $z = 0.85$  m.

675

### 676 **Wind measurements and analysis**

677

678 The wind sensor (WS) consists of 2 horizontal booms placed on the RSM 1.5 m above  
679 the rover base, and rotated in azimuth 120 degrees with respect to each other.

680

681 This placement allows at least one of them to be out of thermal disturbance and out of  
682 the rover geometry for any wind direction. Therefore, the level of confidence and the  
683 analysis of the perturbing effect that the rover causes on the measurements made will  
684 properly depend on the wind direction and speed.

685

686 Thus, the global data retrieval procedure implemented on the ground consists of the  
687 weighted combination of the local wind speed retrievals from each individual sensor,  
688 thereby obtaining the free-flow wind estimate. The weighting of each contribution is  
689 established based on the results of the computational fluid dynamic models developed  
690 to evaluate how the free wind flow is affected by the rover hardware, thus allowing  
691 interpretation of the local wind measurements at each boom location. More details of  
692 this process are provided in [2].

693

### 694 **SkyCam image analysis**

695

696 SkyCam imager is integrated inside the RDS sensor (described above), and permanently  
697 pointed at the Martian sky. The orientation of the camera is not motorized, and its optics  
698 are fixed.

699 SkyCam optical depths were measured via extinction determined through direct solar  
700 imaging [2]. The image field of view includes a neutral density 5 annulus: when the Sun  
701 is within the annulus twice each sol, it appears comparable in brightness to the sky  
702 outside the annulus. Flux from the Sun was integrated after removal of background  
703 signal (mostly dark current). From the flux and atmospheric path at the time of each  
704 image, optical depth is calculated as:  $\tau = \text{alog}(F/F_0)/\eta$ , where  $\tau$  is normal optical depth,  
705  $F$  is observed solar flux,  $F_0$  is a calibration parameter representing solar flux in the  
706 absence of an atmosphere, and  $\eta$  is airmass, which is the ratio of atmospheric column-  
707 mass on the observed ray to normal column-mass. Because SkyCam cannot be calibrated  
708 by observing a wide range of airmasses or changing the camera vs. atmosphere

709 geometry [24] it was calibrated by comparison to MastCam-Z-derived optical depths  
710 [19].

711 The current estimates of SkyCam opacity uncertainties are 0.07 and do not vary much  
712 among points. The estimates for the AM-PM difference is about  $\sim 0.05$ . Also, since the  
713 systematic error dominates, averaging points results in only a small change in  
714 uncertainty.

715

## 716 **Surface Energy Budget. Derivation and importance**

717

718 MEDA allows for the first in situ quantification of the Surface Energy Budget (SEB) on  
719 Mars. To this end, conservation of energy at the surface–atmosphere interface of Mars  
720 requires that

721

$$722 \quad G = (SW_d - SW_u) + (LW_d - LW_u) + T_f - L_f \quad (1)$$

723

724 where  $G$  represents the net heat flux into the ground,  $SW_d$  the downwelling solar flux,  
725  $SW_u$  the solar flux reflected by the surface,  $LW_d$  the downwelling longwave atmospheric  
726 flux,  $LW_u$  the upwelling longwave flux emitted by the surface,  $T_f$  the turbulent heat flux,  
727 and  $L_f$  the latent heat flux. By convention, radiative fluxes directed toward the surface  
728 (warming) and nonradiative fluxes ( $T_f$ ,  $L_f$ , and  $G$ ) directed away from the surface (cooling)  
729 are taken positive in Eq. 1. Moreover, the radiative fluxes are plugged into Eq. 1 as  
730 positive values, whereas nonradiative fluxes can be plugged in as positive or negative  
731 depending on whether they are directed away from or toward the surface.

732

733 RDS measures  $SW_d$  between 0.2 and 1.2  $\mu\text{m}$ , while TIRS measures  $SW_u$  between 0.3 and  
734 3  $\mu\text{m}$ , and  $LW_d$  and  $LW_u$  between 6.5 and 30  $\mu\text{m}$  [2-33-34]. As required in quantifications  
735 of the SEB, measured radiative fluxes must be extended to the entire shortwave (0.2 –  
736 5  $\mu\text{m}$ ) and longwave (5 – 80  $\mu\text{m}$ ) ranges. To extend  $SW_d$  and  $SW_u$ , we use the radiative  
737 transfer model COMIMART [11] along with measured values of aerosol optical depth  
738 from the MastCam-Z instrument [17]. We note that the incoming radiation between 0.2  
739 and 1.2  $\mu\text{m}$  accounts for around 78% of the entire shortwave flux, and that the  
740 uncertainty in this extension is small because COMIMART includes wavelength-  
741 dependent dust radiative properties, accounting for the variations (smaller than 3% for  
742 the majority of conditions) in the conversion factor as a function of dust opacity and  
743 solar zenith angle. Similarly, we assume a surface emissivity,  $\epsilon$ , of 0.99 and the Stefan-  
744 Boltzmann law to extend  $LW_u$ . This value of  $\epsilon$  minimizes the difference between the  
745 ground temperature measured by TIRS (8 – 14  $\mu\text{m}$ ) and the ground temperature derived  
746 from  $LW_u$ . To extend  $LW_d$ , we use the University of Helsinki/Finnish Meteorological  
747 Institute adsorptive Subsurface–atmosphere Column Model (SCM) along with measured  
748 values of aerosol optical depth [32]. Fig. 1a showed the diurnal evolution of each term  
749 of the SEB terms on a particular sol, both obtained from MEDA (symbols) and simulated  
750 by SCM (solid lines). Extended Data Fig. 2 shows the evolution of these magnitudes  
751 recorded by MEDA over the first 250 sols. The excellent agreement demonstrates that  
752 MEDA’s measurements are robust.

753

754 The turbulent heat flux is defined as  $T_f = \rho_a c_p \overline{w'T'}$ , where  $\rho_a$  is the air density,  $c_p = 736$   
 755  $J/Kg \cdot K$  is the specific heat of CO<sub>2</sub> gas at constant pressure, and  $\overline{w'T'}$  is the covariance  
 756 between turbulent departures of the vertical wind speed,  $w'$ , and temperature,  $T'$ . These  
 757 departures are typically calculated over periods of about a few minutes [15]. As MEDA  
 758 measurements of  $w$  are not yet available, we use the drag transfer method to indirectly  
 759 calculate the turbulent heat flux as:

760

$$761 \quad T_f = k^2 U_a \rho_a c_p f(R_B) \frac{(T_g - T_a)}{\ln^2(z_a/z_0)} \quad (2)$$

762 where  $k = 0.4$  is the von Karman constant,  $z_a = 1.45$  m is the height at which the air  
 763 temperature and horizontal wind speed ( $U_a$ ) are measured,  $z_0$  is the surface roughness  
 764 (set to 1 cm [35]), and  $f(R_B)$  is a function of the bulk Richardson number that accounts  
 765 for the thermal stability in the near surface of Mars [36].

766

767 We note that  $L_f$  has been neglected in the SEB because formation or sublimation of  
 768 surface ice has not been detected at Jezero to date, with maximum near-surface relative  
 769 humidity values below 25% for the first 250 sols.

770

### 771 Derivation of Thermal Inertia using MEDA measurements

772

773 We use MEDA measurements of the SEB as the upper boundary condition to solve the  
 774 heat conduction equation in the soil for homogeneous terrains:

775

$$776 \quad \frac{\partial T(z,t)}{\partial t} = \left( \frac{TI}{\rho c_p} \right)^2 \frac{\partial^2 T(z,t)}{\partial z^2} \quad (3)$$

$$777 \quad -\frac{TI}{\rho c_p} \frac{\partial T(z=0,t)}{\partial z} = G = (SWd - SWu) + (LWd - LWu) + Tf - Lf \quad (4)$$

$$778 \quad T(z = z_d, t) = T_d, \quad (5)$$

779

780 where TI is the thermal inertia,  $\rho$  is the soil density,  $c$  is the soil specific heat, and  $z_d$  is  
 781 the depth at which the subsurface temperature is constant and equal to  $T_d$ . Here, we

782 assume that  $\rho c = 1.2 \times 10^6 J \cdot m^{-3} \cdot K^{-1}$  and  $z_d = 3 \times L$ , where  $L = \left( \frac{TI}{\rho c} \right) \sqrt{\frac{2}{\omega}}$  is the diurnal e-  
 783 folding depth and  $\omega = 7.0774 \times 10^{-5} s^{-1}$  is the angular speed of Mars' rotation.

784

785 Under these assumptions,  $T_d$  and TI are the only unknowns, which can be solved by best  
 786 fitting the solution to Eqs. 3–5 to measured values of the daily minimum ground  
 787 temperature and diurnal amplitude in ground temperature, respectively. As analyzed in  
 788 [37] the solution to Eqs. 3–5 depends primarily on TI, with significantly smaller variations  
 789 as a function of  $T_d$ ,  $z_d$  and  $\rho c$ .

790

### 791 Data availability

792  
793 All datasets of Mars2020 are available via the Planetary Data System (PDS). Data are  
794 delivered to the PDS according to the Mars2020 Data Management Plan available in the  
795 Mars2020 PDS archive.

796  
797 Data from the MEDA instrument referenced in this paper are available from the PDS  
798 Atmospheres node. The direct link is [https://pds-  
799 atmospheres.nmsu.edu/data\\_and\\_services/atmospheres\\_data/PERSEVERANCE/meda.  
800 html](https://pds-atmospheres.nmsu.edu/data_and_services/atmospheres_data/PERSEVERANCE/meda.html)

801

## 802 **Acknowledgments**

803

804 This work has been funded by the Spanish Ministry of Economy and Competitiveness,  
805 through the projects No. ESP2014-54256-C4-1-R (also -2-R, -3-R and -4-R); Ministry of  
806 Science, Innovation and Universities, projects No. ESP2016-79612-C3-1-R (also -2-R and  
807 -3-R); Ministry of Science and Innovation, projects No. ESP2016-80320-C2-1-R, RTI2018-  
808 098728-B-C31 (also -C32 and -C33), RTI2018-099825-B-C31 and PID2019-109467GB-I00;  
809 Instituto Nacional de Técnica Aeroespacial; Ministry of Science and Innovation's Centre  
810 for the Development of Industrial Technology; Spanish State Research Agency (AEI)  
811 Project MDM-2017-0737 Unidad de Excelencia "María de Maeztu"- Centro de  
812 Astrobiología; Grupos Gobierno Vasco IT1366-19; and European Research Council  
813 Consolidator Grant no 818602.

814

815 The US co-authors performed their work under sponsorship from NASA's Mars 2020  
816 project, from the Game Changing Development program within the Space Technology  
817 Mission Directorate and from the Human Exploration and Operations Directorate. Part  
818 of this research was carried out at the Jet Propulsion Laboratory, California Institute of  
819 Technology, under a contract with the National Aeronautics and Space Administration  
820 (80NM0018D0004).

821

822 Germán Martínez wants to acknowledge JPL funding from USRA Contract Number  
823 1638782.

824

## 825 **Author contributions**

826

827 J.-A.R.-M. is the PI of the MEDA instrument, and together with M.T.J. and A.S.L., the  
828 three are the corresponding authors of this manuscript, having coordinated,  
829 conceptualized this work, and analyzed the data received. R.H., A.M., T.dR.-G. and A.L.  
830 have contributed with the analysis of the thermal, pressure and wind data, mainly. G.M.,  
831 E.S., A.dV.R., M.S., M.R., H.S. and O.P. have focused their work on the calibration and  
832 analysis of the data recorded by TIRS and some RDS channels, and the modeling of the  
833 SEB estimation, as well as the thermal inertia and albedo studies. M.T.L. and M.W. have  
834 led the analysis of the OD from the images taken by MEDA. C.E.N., D.V.-M., J.G.-E., J.P.-  
835 G., R.S., M.I.R. and S.C.R. have analyzed the wind data, and used different numerical  
836 simulation models to support the global and mesoscale meteorological studies. M.H.,  
837 L.T., J.P., I.J., M.G., A.-M.J. and T.M. have calibrated and analyzed pressure and humidity

838 sensor data in support of the presented studies. D.T., V.A., I.A., J.B., J.-J.J. and A.S.-L. are  
839 focusing their efforts on RDS data analysis, sensor calibration, and field campaigns in  
840 support of cloud studies, dust devil detection and photochemistry. P.G.C., F.G.G. and  
841 A.F. contribute to the relational study between atmospheric dynamics and  
842 astrobiological ground conditions relevant to the potential (extinct) life. N.M.  
843 contributes to the comparative study of atmospheric turbulence from MEDA data and  
844 those recorded by the microphone of the SuperCam instrument. S.N., J.T., M.M., S.G.,  
845 J.C., M.D.-P., S.E. and V.J. have contributed to the design, continuous calibration, data  
846 analysis and event analysis of the WS. J.M.-S., J.R., R.F., I.P.-G., J.T.S., M.G.-V. and M.P.  
847 have contributed to the design and operation of the ATS. V.P.-G., L.M.-S. and R.U.  
848 coordinate the overall daily operation of the instrument. D.B., A.B., K.R., S.G. and E.F.  
849 participate in the scientific planning of the instrument activities, analyze the recorded  
850 data, and take part in the discussion of the atmospheric campaigns to be performed.  
851 S.Z., A.M., C.M. and C.R. take part in the daily operation of the instrument, an essential  
852 task for obtaining the analyzed data. In short, all authors contributed to the  
853 investigations, analyzed part of the data recorded by MEDA and reported in this paper,  
854 and provided material and comments in the process of writing this paper.

855

**856 Competing interests**

857

858 The authors declare no competing interests.

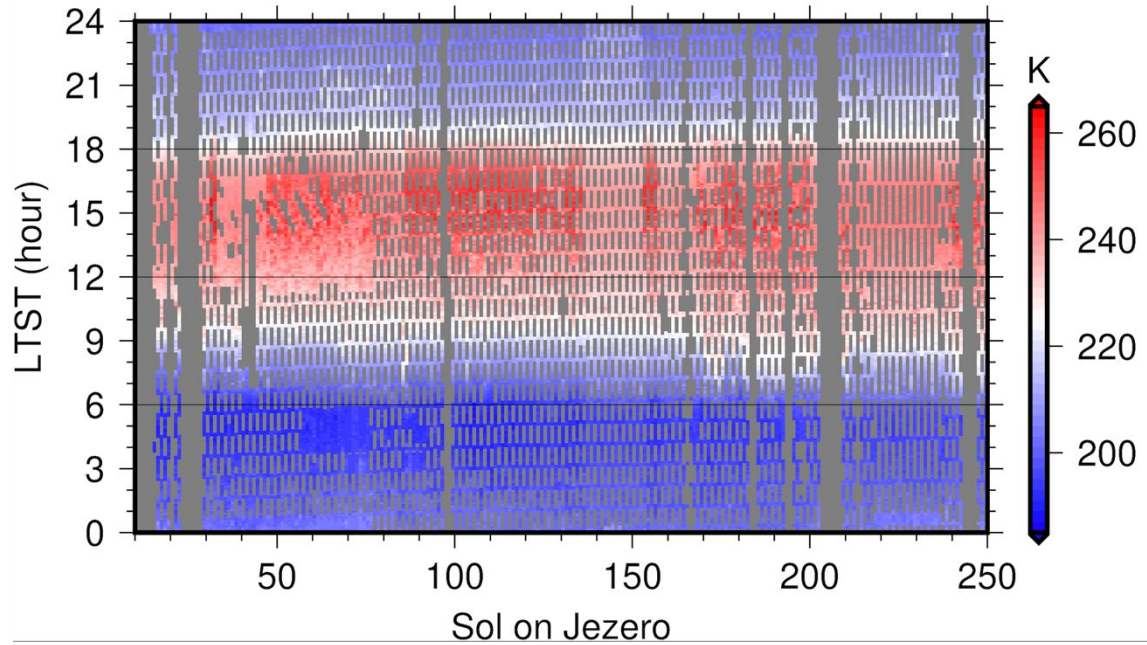
859 **Extended Data Figures**

860

861 **Extended Data Fig. 1**

862

863



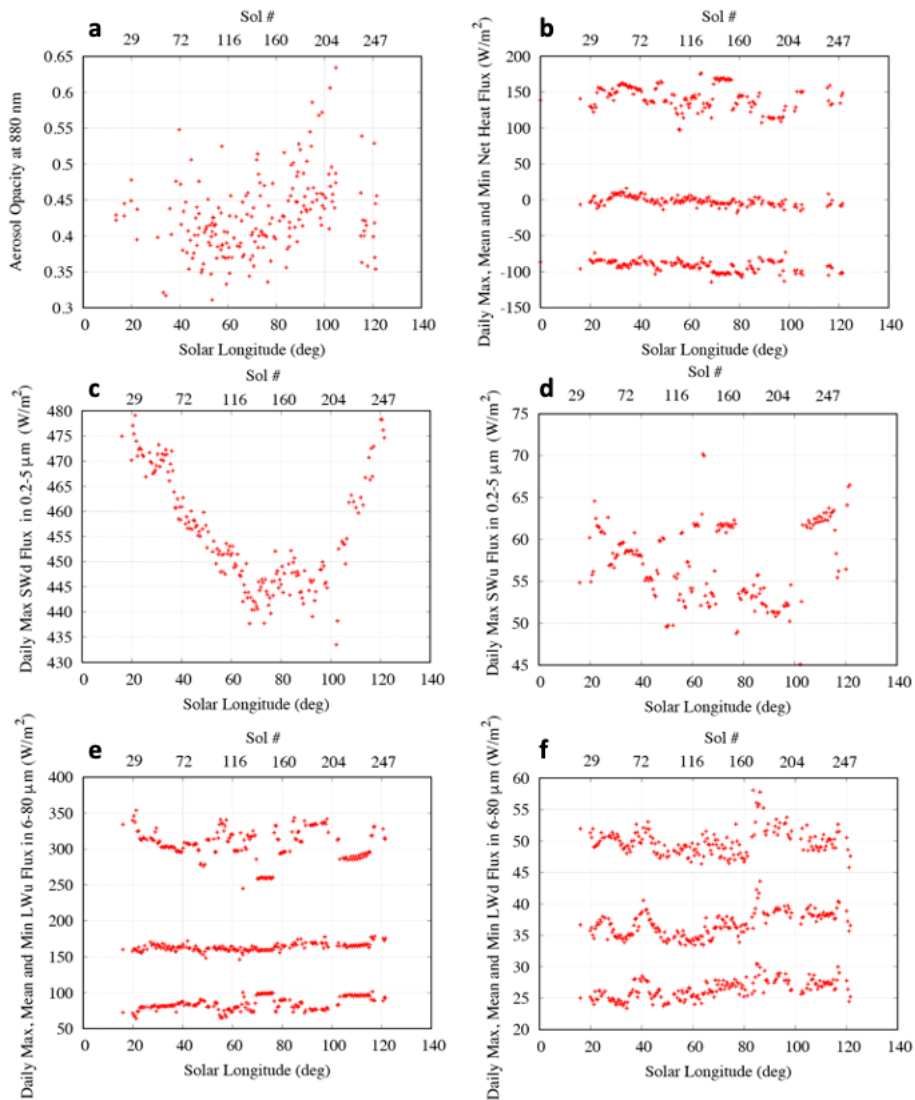
864

865 *Extended Data Fig. 1. Temporary coverage during the first few sols of Perseverance on the surface of Mars showing,*  
866 *as an example, one of the magnitudes recorded by the instrument. Blank periods correspond to situations of mission*  
867 *necessity (start-up, software updates, etc.), or to a specific incident that has occurred to the instrument. The color*  
868 *code corresponds to the temperature recorded by the air temperature sensor (ATS) at  $z = 1.45$  m, averaged every 5*  
869 *minutes.*

870

871 **Extended Data Fig. 2**

872



873

874

875

876

877

878

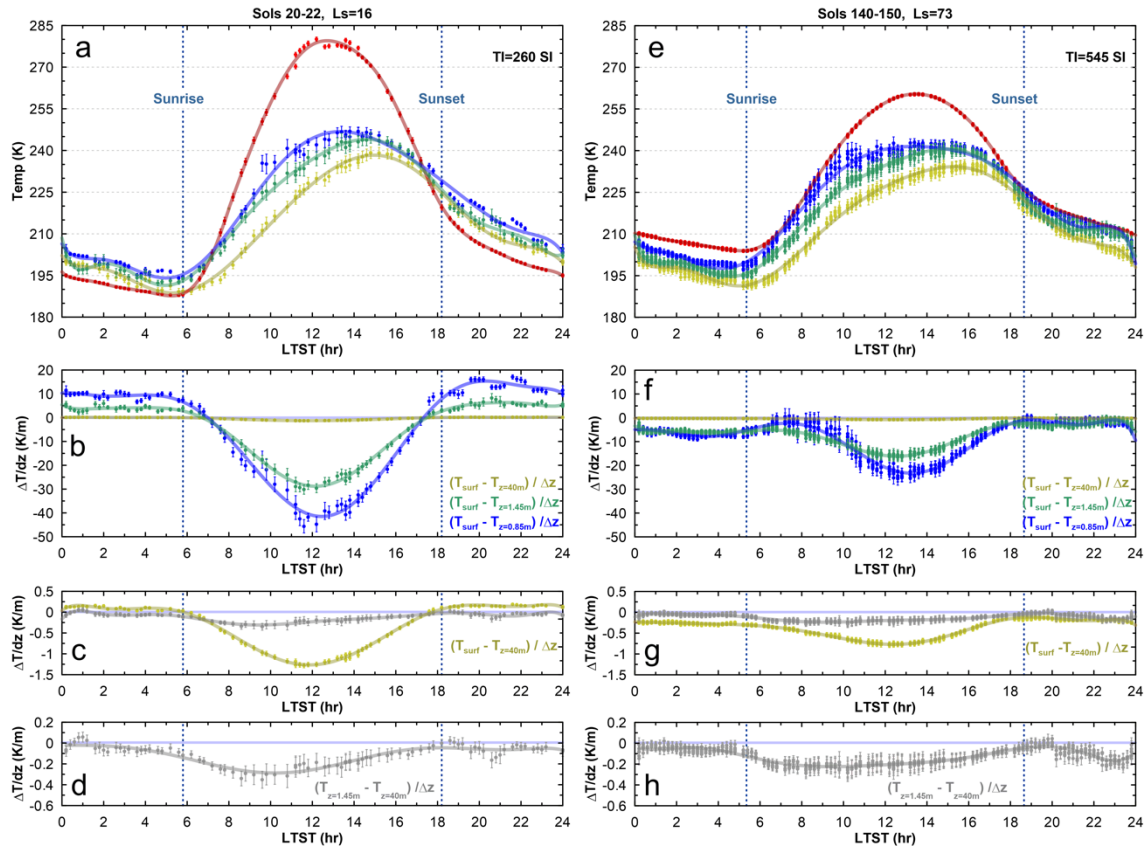
879

Extended Data Fig. 2. Seasonal evolution for the first 250 sols of the M2020 mission of: **(a)** the atmospheric opacity at 880 nm retrieved from MastCam-Z; **(b)** daily maximum, mean and minimum values of the net heat flux into the soil ( $G$ ); **(c)** daily maximum downwelling solar flux in the  $0.2-5 \mu m$  range ( $SW_d$ ); **(d)** daily maximum solar flux in the  $0.2-5 \mu m$  range reflected by the surface ( $SW_u$ ); **(e)** daily maximum upwelling longwave flux in the  $6-80 \mu m$  range emitted by the surface ( $LW_u$ ); and **(f)** daily maximum downwelling atmospheric longwave flux in the  $6-80 \mu m$  range ( $LW_d$ ). All these values were calculated as described in the Methods section.

880

881 **Extended Data Fig. 3**

882



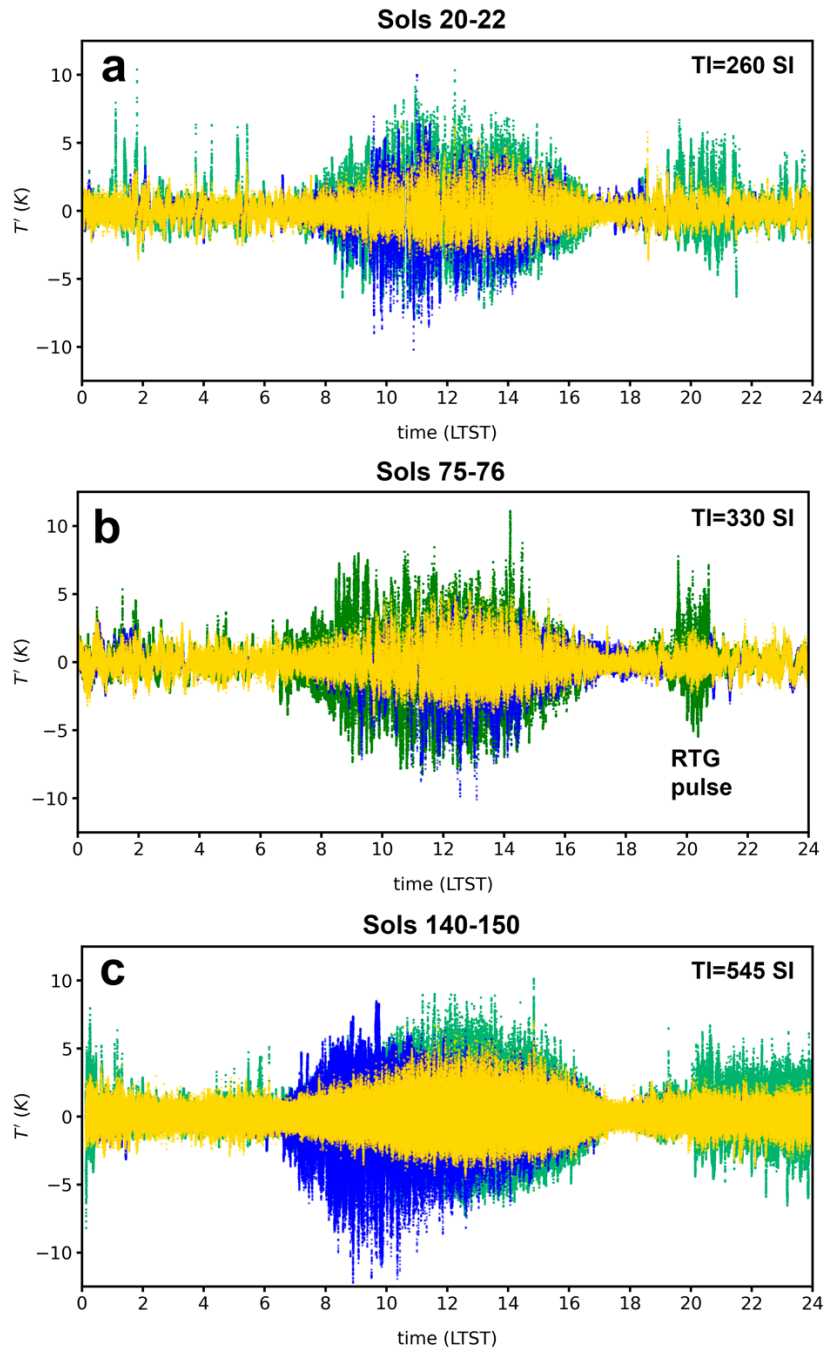
883

884 *Extended Data Fig. 3. Daily Cycle of temperatures at Jezero under low and high values of TI of the local terrain, and*  
 885 *thermal gradients of the atmosphere. (a-d) Low thermal inertia with  $TI = 260 \text{ J}\cdot\text{m}^{-2}\cdot\text{K}^{-1}\cdot\text{s}^{-1/2}$ , as in sols 20-22. (e-h) High*  
 886 *thermal inertia terrain with  $TI = 545 \text{ J}\cdot\text{m}^{-2}\cdot\text{K}^{-1}\cdot\text{s}^{-1/2}$ , as in sols 140-150. Colors legend is as in Fig. 2. Low surface thermal*  
 887 *inertia (left panels) result in more stable conditions than high values of the surface thermal inertia. However this is*  
 888 *mainly due to the strong locality of the surface temperatures compared to a more constant behavior of temperatures.*

889

890 **Extended Data Fig. 4**

891



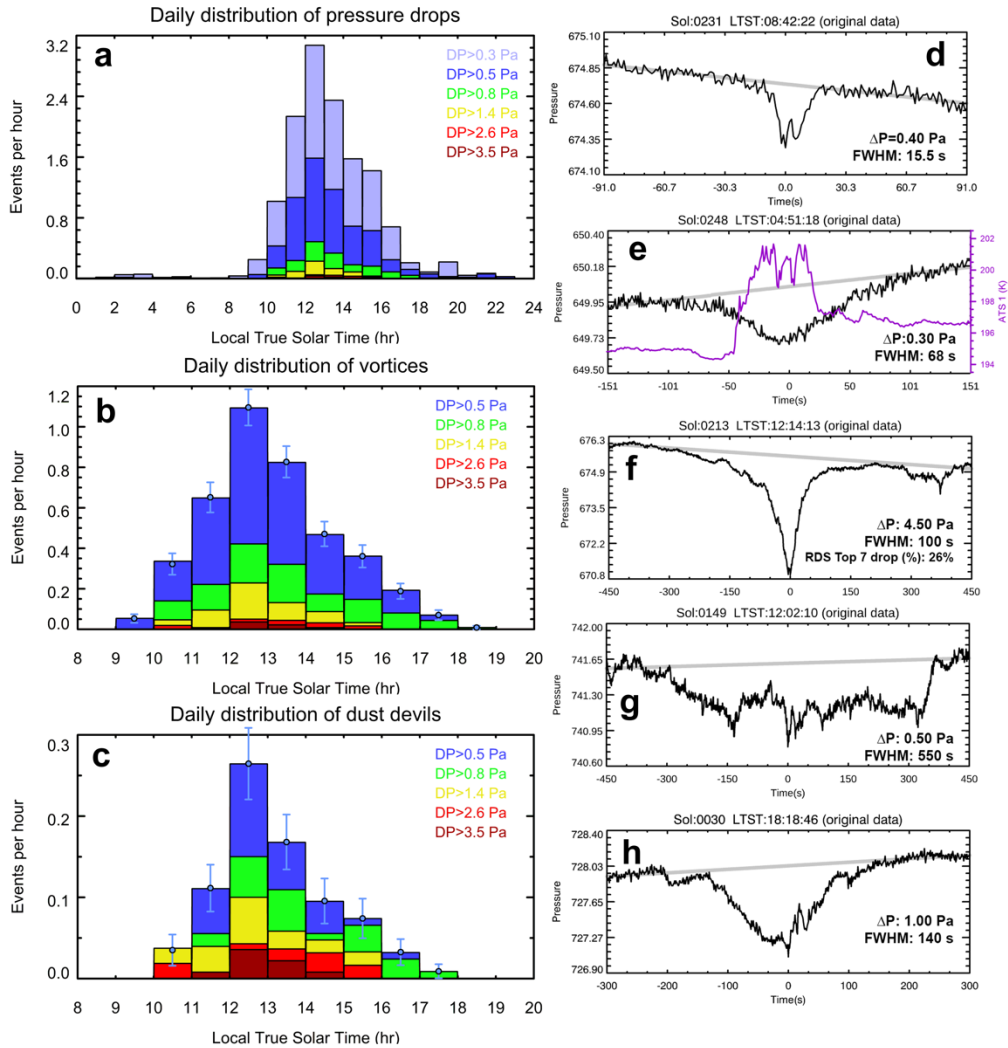
892

893 *Extended Data Fig. 4. Analysis of thermal oscillations along the sol, for the periods (a) sols 20-22, (b) sols 75-76, (c)*  
 894 *sols 140-150, corresponding to different TI values. Blue dots correspond to ATS measurements at  $z = 0.84 \text{ m}$ , green*  
 895 *dots to ATS measurements at  $z = 1.45 \text{ m}$ , and yellow dots to TIRS measurements at  $z \sim 40 \text{ m}$ . The large amplitudes*  
 896 *around 20:00 h correspond to thermal contamination by the RTG at that time, as confirmed by simultaneous wind and*  
 897 *rover yaw. The oscillations were calculated by detrending the temperature data in each half-hour period using a 2<sup>nd</sup>*  
 898 *order polynomial.*

899

900 **Extended Data Fig. 5**

901



902

903

904

905

906

907

908

909

910

911

912

913

*Extended Data Fig. 5. Pressure drops on MEDA data. (a) Daily distribution of pressure drops identified using the algorithm described in [13]. (b) Selection of events with at least a pressure drop of 0.5 Pa and a pressure curve compatible with a vortex after visualization of each individual event. (c) Selection of events in (b) that also have a simultaneous drop in the light measured by the RDS Top\_7 photodiode with a drop of at least 0.5%. Histograms have been corrected from sampling effects. Error bars were evaluated using Monte-Carlo simulations considering the number of detections and hours of observations. (d-h) Examples of a variety of pressure drops including: (d) weak vortices typical of the early morning; (e) night-time pressure drops coincident with increases in temperature and driven by thermal pulses from the RTG when the wind flows from the back of the rover to the Remote Sensing Mast (wind data not shown); (f) the most dusty event captured in the first 250 sols, also one of the most intense and longest; (g) long and noisy pressure drops typically found at noon and suggestive of the passage of the boundaries of convective cells; (h) long vortex just after sunset. Further information on events like (f) and (g) is given in [20].*

914

915

916 **References**

917

918 30. Edwards, C.S., P.R. Christensen, G.L. Mehall, S. Anwar, E. Al Tunaiji, K. Badri, et al.,  
 919 2021. The Emirates Mars Mission (EMM) Emirates Mars InfraRed Spectrometer (EMIRS)  
 920 Instrument. *Space Sci. Reviews.*, 217:77, doi: 10.1007/s11214-021-00848-1.

921

922 31. Apestigue, V., Gonzalo, A., Jimenez, J.J., Boland, J., Lemmon, M., de Mingo, J.R.,  
 923 Garcia-Menendez, E., Rivas, J., Azcue, J., Bastide, L., Andres, N., Martinez-Oter, J.,  
 924 Gonzalez-Guerrero, M., Martin-Ortega, A., Toledo, D., Alvarez-Rios, F.J., Serrano, F.,  
 925 Martin, B., Manzano, J., Lopez-Heredero, R., Carrasco, I., Aparicio, S., Carretero, A.,  
 926 MacDonald, D.R., Moore, L.B., Alcacera, M.A., Fernandez-Viguri, J.A., Martin, I., Yela, M.,  
 927 Alvarez, M., Manzano, P., Martin, J.A., del Hoyo, J.C., Reina, M., Urqui, R., Rodriguez-  
 928 Manfredi, J.A., de la Torre Juarez, M., Hernandez, C., Cordoba, E., Leiter, R., Thompson,  
 929 A., Madsen, S., Smith, M.D., Viudez-Moreiras, D., Saiz-Lopez, A., Sanchez-Lavega, A.,  
 930 Gomez-Martin, L., Martinez, G.M., Gomez-Elvira, F.J., Arruego, I. (2022) Radiation and  
 931 Dust Sensor for Mars Environmental Dynamics Analyzer onboard M2020 rover. *Sensors*,  
 932 22, 2907, doi: 10.3390/s22082907.

933

934 32. Savijärvi, H. I., Martinez, G. M., Fischer, E., Rennó, N. O., Tamppari, L. K., Zent, A., &  
 935 Harri, A. M. (2020) Humidity observations and column simulations for a warm period at  
 936 the Mars Phoenix lander site: constraining the adsorptive properties of regolith. *Icarus*,  
 937 343, 113688.

938

939 33. Sebastian, E., Martínez, G.M., Ramos, M., Haenschke, F., Ferrándiz, R., Fernández,  
 940 M., Rodriguez-Manfredi, J.A. (2020) Radiometric and angular calibration tests for the  
 941 MEDATIRS radiometer onboard NASA's Mars 2020 mission, *Measurement* 164, 107968,  
 942 doi: 10.1016/j.measurement.2020.107968.

943

944 34. Sebastián, E., Martínez, G., Ramos, M., Pérez-Grande, I., Sobrado, J., & Manfredi, J.  
 945 A. R. (2021) Thermal calibration of the MEDA-TIRS radiometer onboard NASA's  
 946 Perseverance rover. *Acta Astronautica*, 182, 144-159.

947

948 35. Hébrard, E., Listowski, C., Coll, P., Marticorena, B., Bergametti, G., Määttänen, A., et  
 949 al. (2012) An aerodynamic roughness length map derived from extended Martian rock  
 950 abundance data. *Journal of Geophysical Research: Planets*, 117(E4). doi:  
 951 10.1029/2011je003942.

952

953 36. Savijärvi, H., and Kauhanen, J. (2008) Surface and boundary-layer modelling for the  
 954 Mars Exploration Rover sites. *Quarterly Journal of the Royal Meteorological Society: A*  
 955 *journal of the atmospheric sciences, applied meteorology and physical oceanography*,  
 956 134(632), 635–641.

957

958 37. Martínez, G.M., Rennó, N., Fischer, E., Borlina, C.S., Hallet, B., De La Torre Juárez, M.,  
 959 and Haberle, R.M. (2014) Surface energy budget and thermal inertia at Gale Crater:  
 960 Calculations from ground-based measurements. *Journal of Geophysical Research:*  
 961 *Planets*, 119(8), 1822-1838.